Temporal DNS of short-wave instabilities in vortex pairs with axial flow.

Nathanael Schaeffer, Clément Roy, Stéphane Le Dizès, Mark C. Thompson

Aeronautics and Space

AST4-CT-2005-012238

FAR-Wake

Fundamental Research on Aircraft Wake Phenomena

Specific Targeted Research Project

Start: 01 February 2005
Duration: 40 months

Temporal DNS of short-wave instabilities in vortex pairs with axial flow

Prepared by: **N. Schaeffer** **(CNRS-IRPHE)**
C. Roy **(CNRS-IRPHE)**
S. Le Dizès **(CNRS-IRPHE, lead)**
M. C. Thompson **(Monash University, Melbourne)**

Document control data

Deliverable No.:	**TR 1.2.1 - 3**	Due date:	**January 2008 (m36)**
Version:	**1.0**	Task manager:	**S. Le Dizès**
Date delivered:	**15 May 2008**	Project manager: EC Officer:	**T. Leweke** **S. Stoltz-Douchet**

Project co-funded by the European Commission within the Sixth Framework Programme (2002-2006)		
Dissemination Level		
PU	Public	×
PP	Restricted to other programme participants (including the Commission Services)	
RE	Restricted to a group specified by the consortium (including the Commission Services)	
CO	Confidential, only for members of the consortium (including the Commission Services)	

Temporal DNS of short-wave instabilities in vortex pairs with axial flow

By Nathanaël Schaeffer[1], Clément Roy[1], Stéphane Le Dizès[1] and Mark Thompson[2]

[1]IRPHE, CNRS, 49 rue F. Joliot Curie, F-13013 Marseille
[2]FLAIR, Department of Mechanical Engineering, Monash University, Melbourne, Victoria 3800, Australia

(Received 15 mai 2008)

In this study, the temporal evolution of the short-wavelength elliptic instability is analysed by direct numerical simulations for configurations with or without axial flow. The three-dimensional linear temporal stability properties of a flow composed of two co-rotating Batchelor vortices are first considered. As for the corresponding counter-rotating case, when the axial flow parameter is increased, different instability modes are observed and identified as a combination of resonant Kelvin modes of azimuthal wavenumbers m and $m+2$ within each vortex. In particular, we show that the sinuous mode, which is the dominant instability mode without axial flow, is stabilized in the presence of a moderate axial flow. The effects of Reynolds number and vortex separation distance on the growth rate parameter map are also considered. The nonlinear dynamics of the elliptic instability in the configurations without axial flow of a single strained vortex and of a system of two counter-rotating vortices is then analyzed. We show that although a weakly nonlinear regime associated with a limit cycle is possible, the nonlinear evolution far from the instability threshold is in general much more catastrophic for the vortex. In both configurations, we put forward some evidence of a universal nonlinear transition involving shear layer formation and vortex loops ejection leading to a strong alteration and attenuation of the vortex. Finally, the effect of axial flow on the nonlinear evolution of the elliptic instability is considered. We show that axial flow tends to weaken the nonlinear dynamics of the elliptic instability. For co-rotating vortex pairs, the impact of the elliptic instability on merging is analyzed. With or without axial flow, we demonstrate that elliptic instability always favors merging and makes the resulting vortex weaker and larger. Moreover, we show that for large separation distances, the effect of the elliptic instability without axial flow on merging is stronger.

---

1. Introduction

Large commercial aircrafts are known to create multiple trailing-vortex systems. These vortices can induce large turning moments on aircraft following, which can be particularly dangerous during takeoff and landing. Given the vortex strength scales with aircraft size, the imminent introduction of several new and much larger passenger aircraft, means that this problem is worsening over time, and must be explicitly taken into account of in air-traffic scheduling. From a purely scientific point-of-view, the component vortices take part in a complex dynamical evolution including merging, and the end result is generally a pair of counter-rotating vortices in the far wake. The two co-rotating vortices generated by the tip of the wing and the outer flap constitute the prototype vortex system that provides one motivation for the analysis presented here, although the focus of this study is mainly theoretical. The goal is to provide the three-dimensional instability

characteristics when the two vortices are identical co-rotating Batchelor vortices including axial flow in their cores (q-vortices) and to determine the impact of the instability on vortex merging.

The *two-dimensional* large Reynolds number dynamics of co-rotating vortex pairs is now well-understood. When the vortices are far-apart, their dynamics is well-described by the point vortex approach (Saffman 1992) ; the two vortices remain in equilibrium with each other, and their cores are elliptically deformed owing to the strain field induced by the other vortex (Le Dizès & Verga 2002). When they are positioned closer to each other, equilibrium is no longer possible and the two vortices merge to form a single vortex (e.g. Meunier *et al.* 2005). When the Reynolds number is large, the two-dimensional dynamics is affected by the development of three-dimensional instabilities. Meunier & Leweke (2005) observed experimentally that a sinuous deformation of each vortex core develops and modifies the merging process. This instability is due to the elliptic character of the streamlines and has been observed in several other systems (see Kerswell 2002, for a review and references). A model has been developed for a vortex pair without axial flow by Le Dizès & Laporte (2002). It was demonstrated that the sinuous deformation corresponds to the resonant combination of two stationary Kelvin modes of azimuthal wavenumbers $m = 1$ and $m = -1$. Subsequently, the effect of axial flow on counter-rotating vortices was analyzed in Lacaze *et al.* (2005, 2007). Lacaze *et al.* (2007) considered a pair of counter-rotating Batchelor vortices. They demonstrated that other instability modes with different azimuthal and temporal characteristics were excited when axial flow was added. They were able to show that each instability mode corresponds to a resonant combination of two Kelvin modes of azimuthal wavenumbers m and $m+2$.

The first part of this work naturally follows on from that investigation of the stability of a pair of equi-strength counter-rotating vortices (Lacaze *et al.* 2007) ; however, it extends that analysis in a number of ways. First, the choice of co-rotating vortices means that the individual vortices undergo rotation about their centroid, rather than the pure self-induced translation of the counter-rotating case. The addition of the associated centrifugal/Coriolis terms to the equations of motion complicate the theoretical stability analysis considerably, which is yet to be completed. The present paper investigates the problem using numerical stability analysis, and explicitly investigates the effect of these terms on the stability characteristics. Second, while the theoretical analysis focuses on the resonance between particular pairs of Kelvin modes, at moderate strain rates most of the wavenumber-axial flow parameter space leads to positive growth ; this aspect was not explored. In particular, as pointed out by (Lacaze *et al.* 2007), the theoretical analysis does not take into account the deviations from ellipticity of the vortices or the loss of proportionality of the axial flow and vorticity in the region between the vortices for higher strain rates, which is automatically accounted for by the numerical stability analysis. Surprising the background growth rate can be almost as high as the growth rate corresponding to identifiable resonant interactions. Third, modes with substantial growth in the critical layer are identified.

The nonlinear dynamics of the elliptic instability is not well known. It constitutes the subject of the second part of the present report. Weakly nonlinear theories exist for a single vortex in a strain field (Sipp 2000), and for rotating flow in a cylinder (Waleffe 1989; Eloy *et al.* 2003; Racz & Scott 2008). In an inviscid framework, these theories predict that the nonlinearity should detune the phase of the instability mode and make its amplitude go back to zero. In a cylinder, viscosity changes this picture as fixed point, limit cycle, chaos, or unbounded growth have been shown to become possible dynamical behaviors (Racz & Scott 2008). For a vortex in a strain field, no such predictions are available. For this reason, we first analyze the nonlinear dynamics of the elliptic instability without axial flow in two simple situations : (1) a single vortex in an imposed strain field, (2) two parallel counter-rotating vortices. Our objectives are to understand the nonlinear regime in the first idealized configuration for which linear and weakly nonlinear theories have been developed and then to extend the results to a vortex configuration directly useful for practical applications. The effect of an axial flow on the nonlinear development of the

elliptic instability is analyzed at the end of the report. In addition to the two previously mentioned configurations, we also consider the case of co-rotating vortices in order to characterize the dynamics of vortex merging in the presence of the instability.

The first section of this report has been submitted for publication by the authors of this report (Roy *et al.* 2008). The second section on the nonlinear dynamics has been performed by N. Schaeffer & S. Le Dizès. A part of this work has also been submitted for publication (Schaeffer & Le Dizès 2008).

2. Linear stability of co-rotating vortex pairs

2.1. *Formulation*

2.1.1. *Base flow*

The formulation mainly follows the numerical part of Lacaze *et al.* (2007), except that here we consider co-rotating vortices instead of counter-rotating vortices. We consider as the base flow, the z-independent flow obtained from the two-dimensional interaction of two co-rotating Batchelor vortices. Each Batchelor vortex taken alone is a solution of the Navier-Stokes equations. Its axial velocity and axial vorticity can be written in cylindrical coordinates as

$$\omega_z = \frac{\Gamma}{\pi a^2} e^{-(r/a)^2} \quad ; \quad U_z = \frac{\xi a_0^2}{a^2} e^{-(r/a)^2} \,, \tag{2.1}$$

where the circulation Γ, the axial velocity strength ξ and initial core radius a_0 are constants. The radius $a(t)$ evolves owing to viscous diffusion according to

$$a(t) = \sqrt{4\nu t + a_0^2} \,, \tag{2.2}$$

where ν is the kinematic viscosity.

The sum of two co-rotating Batchelor vortices is not a solution. As explained in Le Dizès & Verga (2002), in the two-dimensional dynamics, there is first a rapid relaxation process during which each vortex equilibrates with the other. In the frame rotating at the angular speed of the two vortices, a quasi-steady solution is reached which subsequently slowly evolves due to viscous diffusion. As long as the system is far from the merging threshold ($a/b < 0.23$), the two vortices remains separated by a constant distance b and rotate around each other at a constant angular speed $\Omega = \Gamma/(\pi b^2)$. Each vortex also feels the strain field induced by the presence of the other vortex. Its streamlines are deformed elliptically at leading order and this makes each vortex sensitive to the elliptic instability. The two-dimensional simulation is necessary to obtain a correct estimate of the strain field within each vortex. In particular, as noted in Le Dizès & Verga (2002), the strain rate at the vortex center is twice as large as obtained from summing the contributions from the two separate Gaussian vortices. What is remarkable is that after the relaxation process (and before merging) the vortex system is mainly characterized by a single parameter a/b where the vortex radius a evolves according to (2.2) as predicted for a single vortex.

The presence of axial flow does not modify these results because the axial flow and axial vorticity dynamics decouple. Moreover, as the axial flow satisfies the same advection-diffusion equation, it remains proportional to the axial vorticity during the whole two-dimensional evolution. In practice, we perform the two-dimensional simulation without axial flow and then add, after the completion of the relaxation process, an axial velocity component such that $U_z(x,y) = \frac{W_0}{2}\omega_z(x,y)$.

After the relaxation period, the radius of each vortex has slightly evolved. It is this new value of a which is taken as the characteristic length scale for the stability analysis. The base flow is then characterized by 3 parameters, a/b, W_0 and the Reynolds number $Re = \Gamma/\nu$, although the base flow is mainly independent of this last parameter.

We shall consider a continuous range of W_0 between 0 and 0.6 for three couples of parameters

($Re = 14000, a/b = 0.14$), ($Re = 14000, a/b = 0.18$) and ($Re = 31400, a/b = 0.168$), and provide some selected results for a few other combinations. For these values of W_0, the Batchelor vortex can be considered as stable. Weakly unstable center modes exist but their growth rate is so small (see Fabre & Jacquin 2004) that they never become dominant over the elliptic instability mode.

2.1.2. *Perturbation analysis*

The stability of three-dimensional modes is examined by linearizing the Navier-Stokes equations written in the frame rotating with the vortices around the frozen base flow. As the base flow is assumed homogeneous in the axial direction, and because the perturbation equations are linear and independent of z for the axial derivatives, the axial dependence can be represented as a Fourier series. Linearity allows the stability of each wavelength, $\lambda = 2\pi/k$, to be determined separately. In practice, for a given axial wavelength, the perturbation equations are integrated in time with a random field as an initial condition. The characteristics of the most unstable mode are obtained by integrating for a sufficiently long time. For each set of base flow parameters and each wavenumber k, we obtain the growth rate, the rotation frequency and the spatial structure of the most unstable mode.

2.1.3. *Numerical codes*

For the linear study, two different numerical codes have been used. The first one was used for a similar study of counter-rotating vortices in Lacaze *et al.* (2007). It is based on a high-order spectral element technique which has been described in Thompson *et al.* (1996) and applied to various related problems (e.g. Thompson *et al.* 2001; Ryan *et al.* 2005). The same code parameters and simulation domain as in Lacaze *et al.* (2007) are used here.

The second code has been developed for the present linear study and the nonlinear analysis presented in the next parts. It is a pseudo-spectral code, periodic in the three spatial Cartesian directions. Such a code is classical (Vincent & Meneguzzi 1991) and has already been used for similar studies (Billant *et al.* 1999; Otheguy *et al.* 2006). Because the code is fully spectral, it is very fast, but is in principle limited to flows with zero total circulation (Pradeep & Hussain 2004). A trick has then to be used to simulate co-rotating vortex pairs for which the circulation is 2Γ : a solid body rotation $\Omega_0 \mathbf{e_z}$ has to be subtracted from the base flow so that the global circulation at the boundary of the domain is zero (see Otheguy *et al.* 2006, for details). Time integration is performed using an Adams-Bashforth temporal scheme. For determining the 2D base flow, the size L of the square domain has been chosen sufficiently large to reduce the influence of image vortices. Typically, we have taken L/b between 5 and 6. A smaller domain with $L'/b \approx 2.5$, centered on the vortex pair has been taken for the simulation of the linear Navier-Stokes equations. This is possible because the perturbations are localized in the center of each vortex and decrease very fast to zero away from the vortices. Thus, there is no difficulty in considering the perturbations periodic on a smaller domain.

The two numerical codes have been compared and validated for a configuration without axial flow. In figure 1 is plotted the growth rate of the perturbations obtained by the two different codes, together with the theoretical formula† given in Le Dizès & Laporte (2002). As it can be seen, the two codes provide the same results for the first three modes. The relative error between the two codes is generally only a few percent. This difference was traced to a slight sensitivity of the growth rate predictions to the time allowed for quasi-equilibrium to be reached before freezing the base flow, which was slightly different for the two cases. On the other hand, the large underestimation of the growth rate by the theoretical formula is due to a incorrect estimate of the damping rate associated with viscous effects. In the theory, the damping rate is based on

† Note that there is a misprint in formula (6.1a) in Le Dizès & Laporte (2002) : b^2/a_1^2 should be b^4/a_1^4.

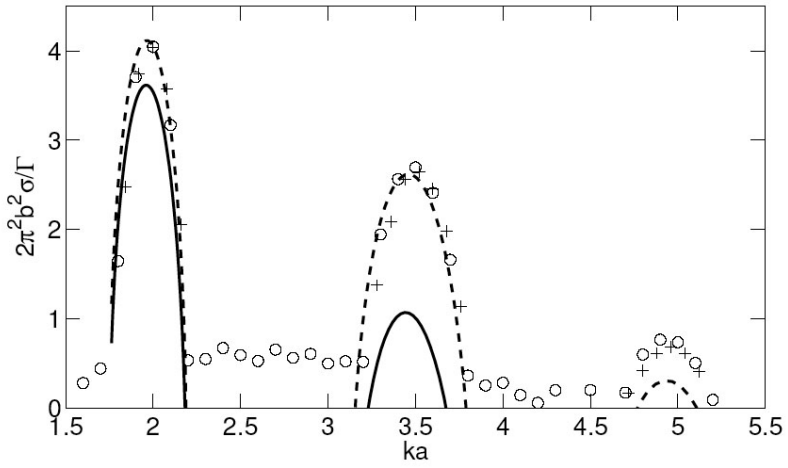

FIG. 1. Comparison of the growth rate computed with the 2 codes for $Re = 14000$ and $a/b = 0.14$. Circles and crosses are data obtained with the fully spectral code and with the spectral-element code respectively. Theoretical predictions are in solid line [formula (6.1a) from Le Dizès & Laporte (2002)], and in dashed line [same formula with a viscous damping term computed by the global approach (see text)].

a local approach. If a global estimate is computed using the method of Lacaze *et al.* (2007), the viscous damping is found to be significantly smaller (Lacaze, private communication) and a much better estimate is obtained. The adjusted theoretical predictions are also shown on this figure by the dashed lines. Note that even this estimate loses accuracy for the higher wavelength mode.

2.2. *Mode map*

Using the procedure explained above, we have first explored a large part of the parameter space for a fixed Reynolds number $Re = 14000$ and $a/b = 0.14$, with a resolution step for W_0 and k of 0.002 and 0.1 respectively. The growth rate contours of the most unstable modes are displayed in figure 2. Only the growth rates (normalized by the turn-over time of the vortex pair) in excess of 0.5 have been indicated in this figure. It demonstrates the existence of several islands of instability. Each island corresponds to a specific instability mode. These modes are localized in the core of each vortex and have the same spatial structure in each vortex. Their spatial structure is shown in figure 3. The characteristics of each mode are also provided in table 1.

The first point to note is that the instability map shown in figure 2 is very similar to the map obtained for equal strength counter-rotating vortices (see figure 11 in Lacaze *et al.* 2007). The first three modes, labeled 1, 2, 3, which have maximum growth rates for no axial flow but persist for small W_0, are the well-known sinuous modes of the elliptic instability (Meunier & Leweke 2005). They correspond to the resonant combination of two Kelvin modes of azimuthal wavenumber $m = 1$ and $m = -1$. Here, the functional dependence of the Kelvin modes is written as $\exp(im\theta + ikz - i\omega t)$ where m and k are the azimuthal and axial wavenumbers, and ω the frequency. Moreover, we assume that k is positive. For $W_0 = 0$, the sinuous modes are stationary ($\omega = 0$) and have been called "principal modes" as they are formed from two Kelvin modes with the same (broad) radial structure. The radial structure of the Kelvin mode can be identified by a label specifying the number of zeros of the radial velocity component of the mode in the vortex core (Lacaze *et al.* 2007). Principal modes are denoted by (m_1, m_2, n) where m_1 and m_2 are the azimuthal mode numbers of the two resonant Kelvin modes and n their common (radial) label. It is possible to identify other resonant modes as combinations of Kelvin modes with different

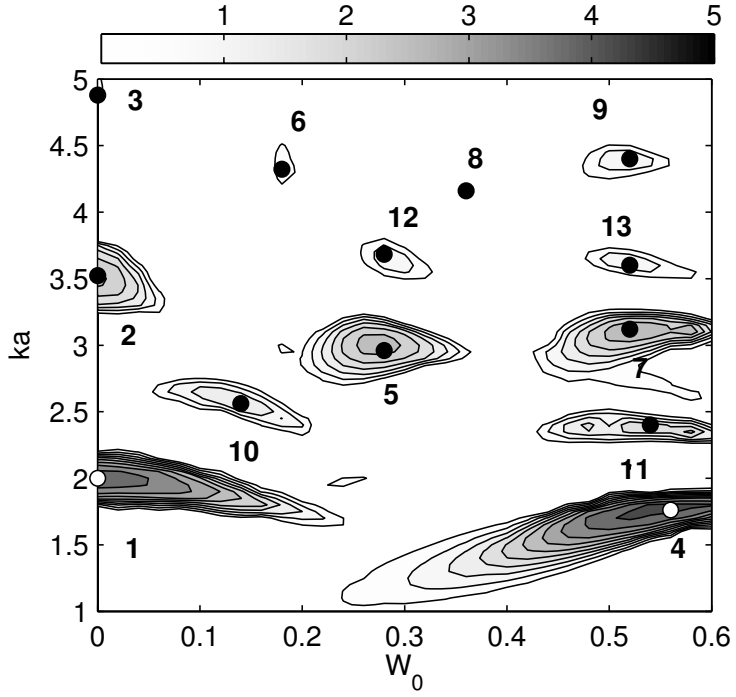

FIG. 2. Contours of instability growth rate in the (W_0, ka) plane for $a/b = 0.14$ and $Re = 14000$. A number has been provided to each important unstable mode and is used hereafter to refer to each of them.

			$Re = 14000$, $a/b = 0.14$				$Re = 14000$, $a/b = 0.18$				$Re = 31400$, $a/b = 0.168$			
mode	m	n	W_0	$\frac{2\pi a}{\lambda}$	$\frac{2\pi^2 b^2 \omega}{\Gamma}$	$\frac{2\pi^2 b^2 \sigma}{\Gamma}$	W_0	$\frac{2\pi a}{\lambda}$	$\frac{2\pi^2 b^2 \omega}{\Gamma}$	$\frac{2\pi^2 b^2 \sigma}{\Gamma}$	W_0	$\frac{2\pi a}{\lambda}$	$\frac{2\pi^2 b^2 \omega}{\Gamma}$	$\frac{2\pi^2 b^2 \sigma}{\Gamma}$
1	-1,1	1	0	2.00	0	4.04	0	1.76	0	5.21	0	1.8	0	5.08
2	-1,1	2	0	3.52	0	2.64	0	3.12	0	4.99	0	3.2	0	4.83
3	-1,1	3	0	4.88	0	0.611	0	4.48	0	4.73	0	4.6	0	4.45
4	0,-2	1	0.56	1.76	-28.8	2.85	0.58	1.68	-15.7	4.81	0.58	1.65	-20.7	4.84
5	0,-2	2	0.28	2.96	-39.1	2.71	0.3	2.88	-20.1	3.74	0.28	2.88	-26.0	4.11
6	0,-2	3	0.18	4.32	-42.3	0.868					0.19	4.11	-27.0	3.39
7	-1,-3	1	0.52	3.12	-84.7	2.88	0.54	3.04	-46.4	3.81	0.55	3	-53.95	4.21
8	-1,-3	2	0.36	4.16	-91.16	0.30					0.37	4.0	-59.8	2.85
9	-2,-4	1	0.52	4.40	-141	1.23					0.53	4.21	-93.6	3.49
10	-1,1	1,2	0.14	2.56	-7.53	1.63	0.1	2.32	-0.59	4.50	0.1	2.4	-0.78	3.42
11	0,-2	1,2	0.54	2.40	-26.3	1.30	0.56	2.24	-15.2	3.06	0.6	2.2	-15.97	3.0
12	0,-2	3,2	0.28	3.68	-37.0	1.21					0.305	3.47	-21.9	3.24
13	-1,-3	1,2	0.52	3.60	-79.1	1.20					0.56	3.4	-48.4	2.84

TAB. 1. Parameters of the modes identified in figures 2, 6 and 7.

radial dependence, in which case the mode is denoted by $(m_1, m_2, [n_1, n_2])$. Examples of these mixed modes can be found in Lacaze *et al.* (2007).

The modes 1, 2 and 3 of figure 2 are the principal modes $(-1,1,1)$, $(-1,1,2)$ and $(-1,1,3)$ respectively. Their spatial structures shown in figures 3(a,b,c) have 1, 2 and 3 radial oscillations as indicated by their radial mode numbers.

For $W_0 = 0$, the numerical growth rate for these modes is in good agreement with the theory

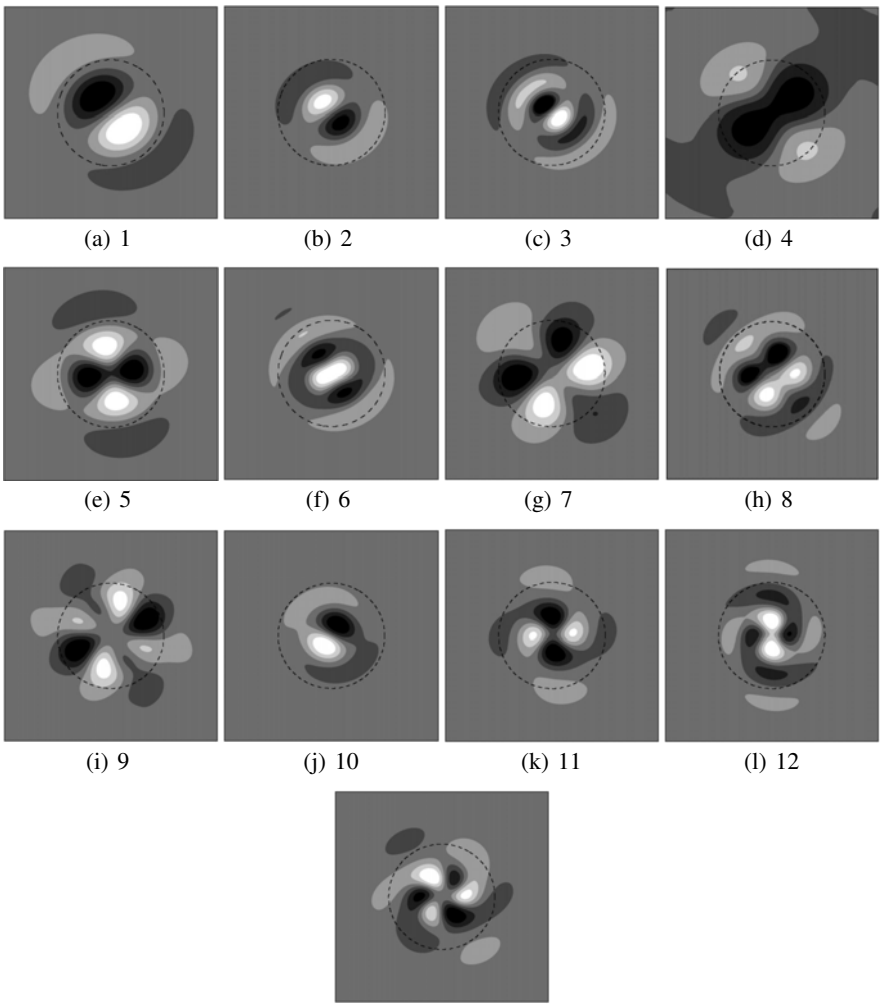

FIG. 3. Axial vorticity perturbation fields resulting from the elliptical instability for $Re = 14000$ and $a/b = 0.14$. Each plot is associated with a number corresponding to one point identified in figure 2. Contours are linear and symmetric around 0. The dashed line is a circle of radius a centered on the vortex center.

[see figure 1]. As the axial flow is progressively increased, these modes are progressively stabilized, as also predicted for counter-rotating vortex configurations (Lacaze *et al.* 2007). As explained in Lacaze *et al.* (2007), this phenomenon has two different causes. First, as soon as an axial flow is present, the symmetry between the $m = 1$ modes and the $m = -1$ modes is broken. The resonance between the two helical modes becomes less efficient because their radial structures are no longer perfectly in phase. Moreover, the symmetry breaking creates a small detuning in the resonant frequency with respect to the frequency which maximizes the local instability in the vortex center. The strength of the local elliptic instability in the vortex center is thus also less important. The second cause is the damping of the Kelvin mode $m = -1$. The damping of this mode is due to the appearance of a viscous critical layer in its radial structure (Le Dizès 2004; Fabre *et al.* 2006). When the damping rate of the mode is greater than the growth rate associated with the resonance, the instability mode disappears.

The other instability modes which are destabilized for larger values of W_0 are no longer sta-

(a) (b) (c)

FIG. 4. Azimuthal decomposition of the instability mode 5 : axial vorticity in a section perpendicular to the vortex axis. (a) Axisymmetric component ($m = 0$), (b) $m = \pm 2$ component, (c) Superposition of $m = 0$ and $m = \pm 2$ components. The circle (solid line) in figures (a) and (b) indicates the position of the turning point r_t (see text).

tionary sinuous modes. The mode labeled 5, corresponds to the principal mode $(-2,0,2)$ which has also been observed in the numerical simulation of counter-rotating vortices. This mode is here the most unstable for $W_0 \approx 0.3$ and $ka \approx 3$. The label of the mode can be obtained by looking at the azimuthal decomposition of the instability mode in one of the vortices as shown in figure 4 for mode 5. The figures 4(a) and 4(b) show the $m = 0$ and the $m = \pm 2$ contribution to this instability mode while figure 4(c) is the superposition of these two contributions alone. We clearly see that the eigenmode shown in figure 3(e) is well reproduced, confirming that mode 5 is mainly a combination of the azimuthal wavenumbers $m = 0$ and $m = \pm 2$. The time evolution and the three-dimensional structure of the mode, which are shown in figures 5(a) and (b) respectively, provide further information on the characteristics of the Kelvin modes involved in the construction of mode 5. We observe that the helical structure is right-hand oriented and rotates anti-clockwise. This indicates that the axial and azimuthal wavenumbers are of opposite sign, and the frequency and azimuthal wavenumber are of the same sign. Thus, our choice of positive k, $m = -2$ and $\omega < 0$ (as indicated in table 1).

The label n of the Kelvin mode involved in the resonance can be obtained by looking at the radial variation of each azimuthal component. Le Dizès & Lacaze (2005) have shown that the label corresponds to the number of radial oscillations between the origin and a turning point r_t which delimits the region where the mode is localized. As explained in Le Dizès & Lacaze (2005), the radial location r_t can be computed from the vortex profile and the characteristics of the mode. The turning point r_t has been indicated for the $m = 0$ and $m = -2$ components of mode 5 in figures 4(a) and 4(b), respectively.

Using a similar azimuthal decomposition and by comparing the figures with the theoretical plot of Lacaze *et al.* (2007), the principal modes $(-2,0,1)$, $(-2,0,3)$, $(-3,-1,1)$, $(-3,-1,2)$ and $(-4,-2,1)$ can be identified with the modes 4, 6, 7, 8 and 9 of figure 2 (see figure 3). Note that an $m = \pm 2$ structure is clearly visible on modes 4 and 6, $m = \pm 3$ structure on modes 7 and 8, and $m = \pm 4$ on mode 9. As expected, the maximum growth rate of the principal modes decreases as their axial wavenumber increases. Other instability modes are also visible in figure 2. They are not principal modes, which means that they involve Kelvin modes with different radial labels. A few of them have been illustrated in figure 3. By looking at the number of oscillations of the main azimuthal components, labels have been tentatively given for each of these modes in table 1.

2.3. *Effects of Reynolds number and vortex separation distance variations*

Similar contour plots to figure 2 are displayed in figures 6 and 7(a) for a/b increased from 0.14 to 0.18 (closer vortices) and a larger Reynolds number (*Re* increased from 14000 to 31400), respectively. A corresponding set of instability modes as shown in figure 2 have also been iden-

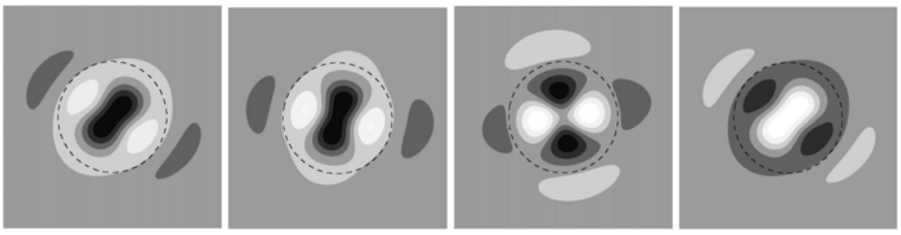

(a)

(b)

FIG. 5. (a) Temporal evolution of the axial vorticity of the instability mode 5 during half a period. Times correspond to 0, $T/8$, $2T/8$, $4T/8$, respectively. (b) Three-dimensional visualization showing an vorticity isosurface indicating the deformation induced by mode 5. Here, the maximum vorticity of the instability mode is 0.4 times the maximum vorticity of the base flow.

tified in these figures. Their characteristics are given in table 1. When a/b is increased, the peaks associated with the main modes move slightly owing to the variation of the mean rotation $(a/b)^2$ of the pair which modifies the conditions of resonance. In particular, the resonant mode positions are shifted to occur at slightly higher axial flow velocities and smaller wavenumbers. For example, for mode 4, an approximately 30% increase in a/b from 0.14 to 0.18, results in a shift in (ka, W_0) coordinates from (1.76, 0.56) to (1.68, 0.58). The relative shift is not uniform across all modes however ; the 30% change in a/b typically leads to approximately a 10% change in ka but only a few percent change in W_0. The position of the peaks is by contrast almost unaffected by variations of the Reynolds number. This is also clearly seen in figure 8(b) where growth rate variations are displayed for a fixed $W_0 = 0.29$ and for various Reynolds numbers.

An important feature of figures 6 and 7(a) is the global increase in the growth rate when either a/b or Re increases. For the range of parameters of these figures, almost the whole parameter space considered is now unstable. However, there are differences between increasing Reynolds number and increasing a/b. When the Reynolds number is increased, the growth rate peaks remain distinct : more modes become unstable but they can still be identified. Note in particular that mode 8, displayed in figure 3(h) and which corresponds to the principal mode $(-1,-3,2)$, is now unstable, whereas it was almost stable for the parameters of figure 2. When a/b increases, the tendency is different. The peaks of the modes for large ka tend to disappear : the growth rate increases almost uniformly as ka increases. The trend is demonstrated in figure 8(a) for a fixed value of $W_0 = 0.29$ for $a/b = 0.18$. In addition, figure 11 shows the behavior for the zero axial velocity case. The growth rate ultimately decreases for large ka, but what is important is that there is no dominant mode selection in that case. Again, this is clearly indicated in figure 6, which shows specific modes are virtually indistinguishable from the background noise for $ka \gtrsim 3.5$ for $a/b = 0.18$. The modes for $ka \gtrsim 3.5$ are apparently mixed and most of them have a spiral-like structure as illustrated in figures 9(a-c).

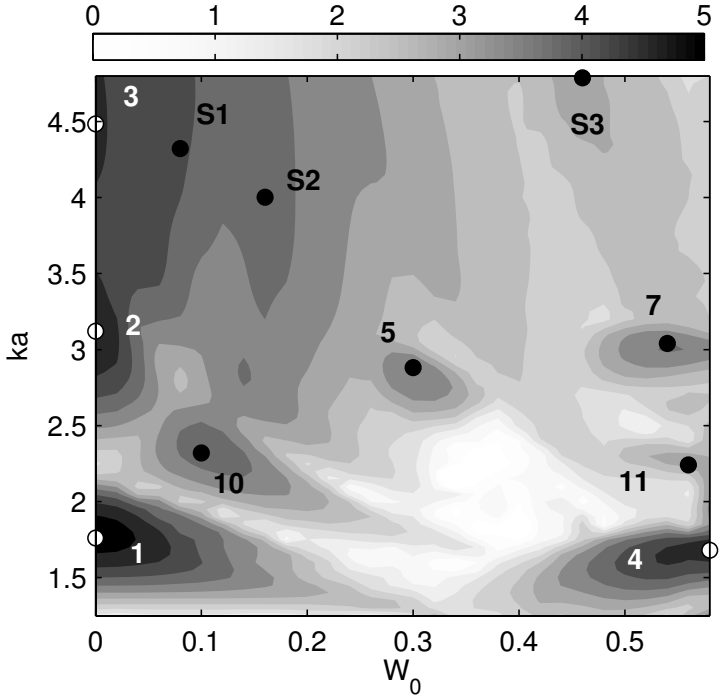

FIG. 6. Same as figure 2 for $a/b = 0.18$ and $Re = 14000$.

The spiral structure is probably associated with a critical layer in one of the resonant modes (Lacaze *et al.* 2007). This critical layer is known to be responsible for the stabilization of some modes, such as the mode $(-1,1,1)$ for increasing W_0. However, for increasing a/b this stabilizing effect becomes less important. Moreover, the instability band also becomes wider and the frequency detuning between modes less important when a/b grows. Thus, we expect that more and more modes would become unstable in larger and larger overlapping instability regions. The consequence is that the growth rate possesses a large growth envelope with no sharp peaks.

2.4. *Comparison of the stability of co- and counter-rotating vortex pairs*

Le Dizès & Laporte (2002) compared the dominant instability modes for co- and counter-rotating vortices for the case without axial flow. In general, the growth rates of instabilities for counter-rotating vortices are lower than for co-rotating vortices and the corresponding wavenumbers of the modes lie between those of the other case. Figure 10 shows growth rate curves for the case without axial flow for $a/b = 0.168$ at $Re = 31400$, which highlights both effects. These predictions are consistent with the analytical and numerical predictions in Le Dizès & Laporte (2002). For the case with axial flow, for which an analytical theory is yet to be developed, figures 7(a) and (b) display the instability maps for the co- and counter-rotating cases for $Re = 31400$ and $a/b = 0.168$. This allows an explicit, albeit numerical, determination of the effect of the added Coriolis force on the stability of co-rotating vortex pairs. As previously mentioned, this difference from the counter-rotating case appears because of the mutually-induced rotation of the each vortex about their centroid, meaning that they appear quasi-stationary in a rotating frame.

There are both similarities and differences between the stability maps. The first point is that a similar set of identifiable modes corresponding to the same Kelvin mode interactions appear on each map in roughly the same locations. However, the actual positions of the modes for the co-rotating vortex map are shifted to approximately 20% higher axial velocities. Another key

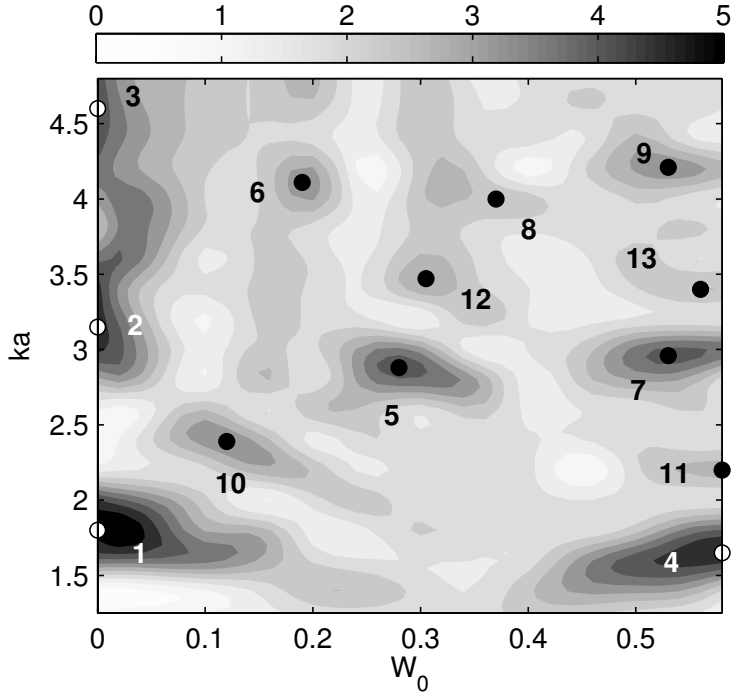

(a)

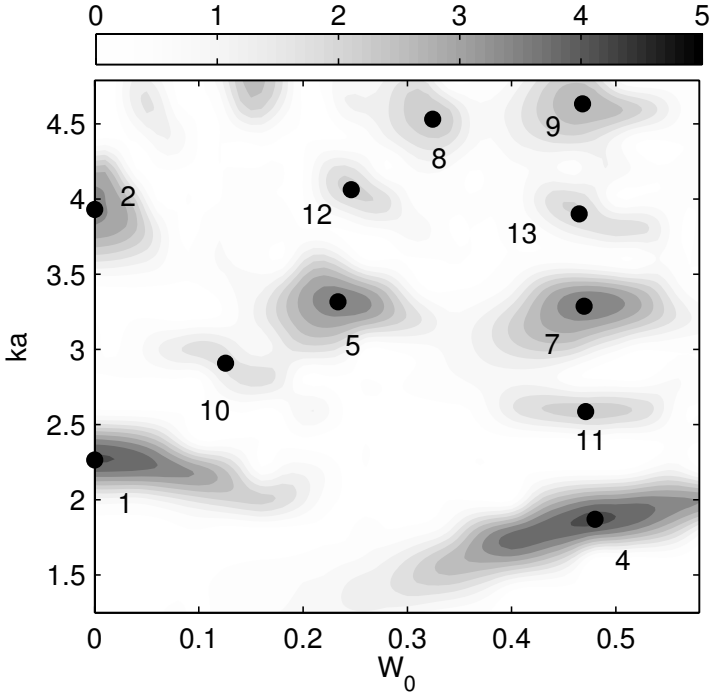

(b)

FIG. 7. As for figure 2 for $a/b = 0.168$ and $Re = 31400$: (a) co-rotating vortices ; (b) counter-rotating vortices

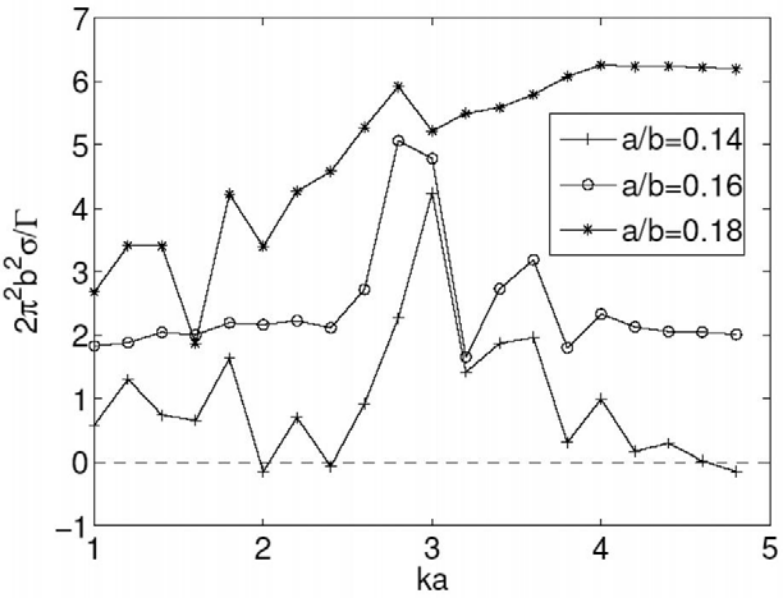

(a)

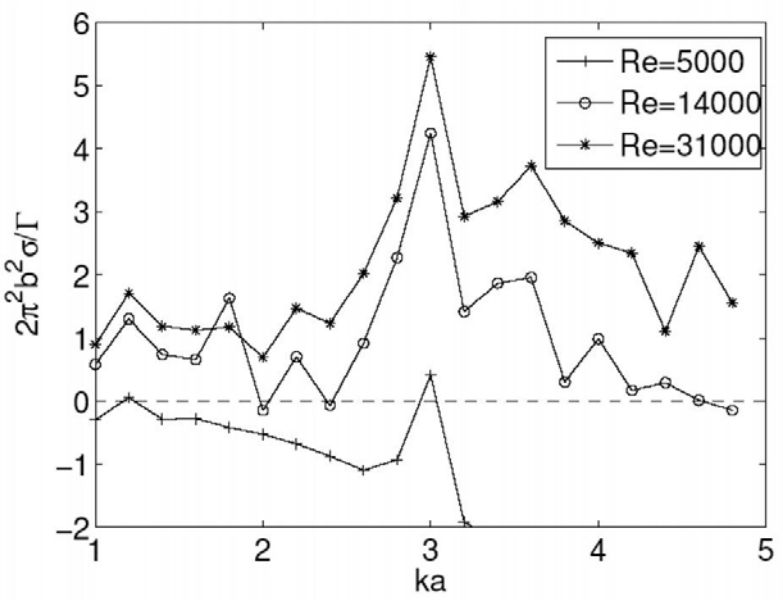

(b)

FIG. 8. Instability growth rate versus axial wavenumber for $W_0 = 0.29$. (a) Vortex separation distance dependence for $Re = 14000$. (b) Reynolds number dependence for $a/b = 0.14$.

difference is the background growth rate between identifiable modes. This is very much larger in the co-rotating case, which is also clear from figure 11 at zero axial flow, which explicitly shows the slow falloff of the growth rate for high wavenumbers.. Indeed, as discussed in the previous section, as a/b is increased to 0.18, the background growth rate virtually swamps the growth rate of local resonant Kelvin mode interactions for higher wavenumbers and may even dominate co-rotating vortex evolution for close vortex cores at particular axial core velocities. This effect

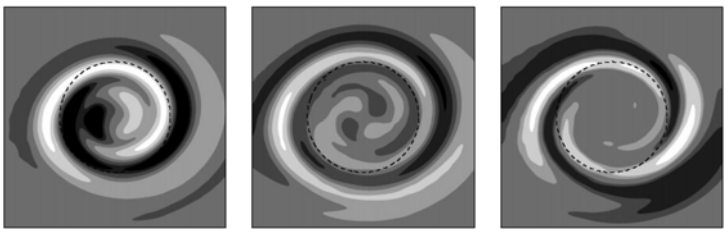

(a) S1 (b) S2 (c) S3

FIG. 9. Instability modes with a critical layer (see fig. 6).

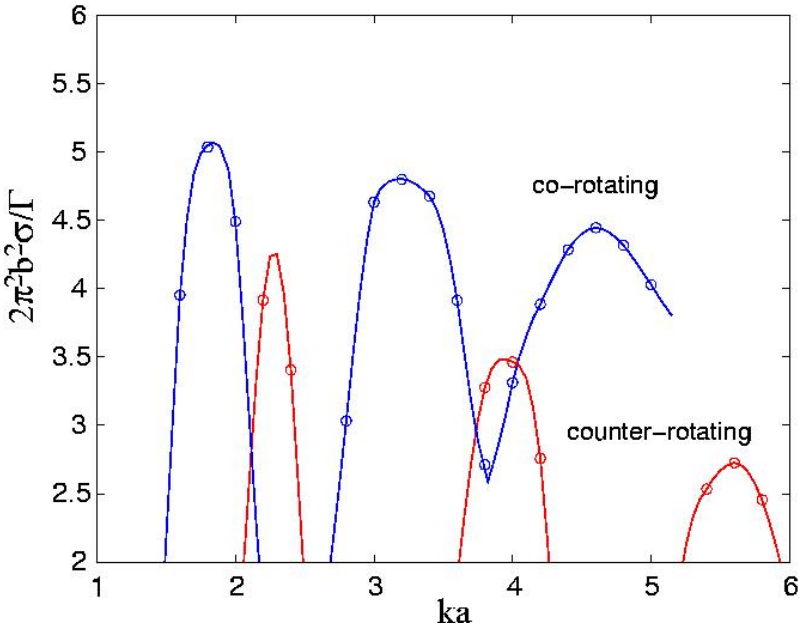

FIG. 10. Comparison of growth rates for equal strength co- and counter-rotating vortices with zero axial velocity for $a/b = 0.168$ and $Re = 31400$.

occurs at separations well under the merging limit for co-rotating vortices of $a/b \simeq 0.23$ (Meunier *et al.* 2005).

3. Nonlinear dynamics of the elliptic instability

3.1. *A single vortex in a strain field and counter-rotating vortices without axial flow*

The nonlinear dynamics of the elliptic instability is examined in this section for two configurations without axial flow : (1) a single vortex in a strain field ; (2) Counter-rotating vortices. For both cases, the nonlinear development of the instability is simulated with the 3D pseudo-spectral Cartesian code which has been used for the linear study. The spatial resolution is typically $256 \times 256 \times 48$ in the (x, y, z) directions where $0z$ is the vortex axis.

The base flow of case (1) is computed using a two-dimensional Navier-Stokes code in cylindrical geometry (finite difference scheme in radial direction and Fourier decomposition in azimuthal direction). This code allows us to impose a fixed strain field for large radial coordinates (fixed here at $R = 15\,a_0$). Starting as initial condition from the axisymmetric Lamb-Oseen vortex plus a uniform strain field of strain rate ε, the flow is found to relax on a non-viscous time scale to

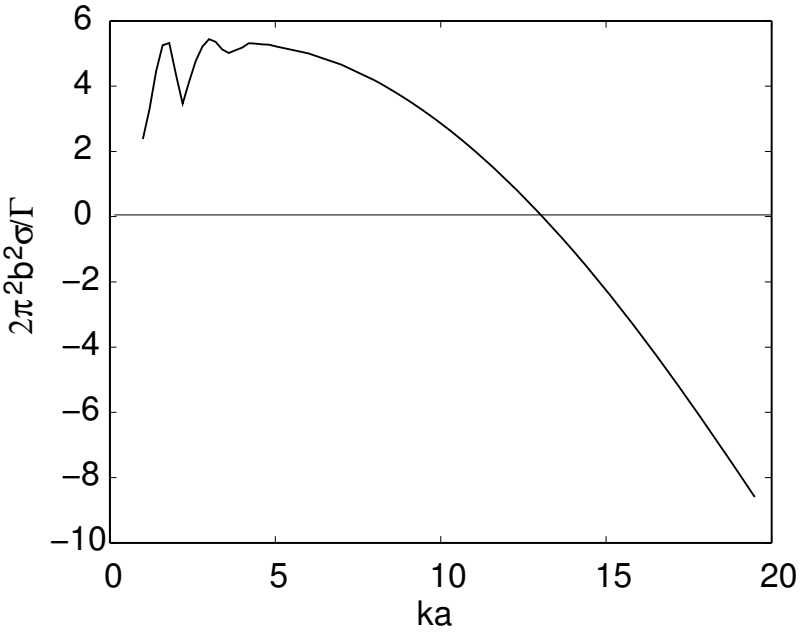

FIG. 11. Growth rate as a function of wavenumber for the case with no axial flow for $Re = 14000$ and $a/b = 0.18$.

the quasi-steady strained vortex solution obtained by Jiménez *et al.* (1996). The good quality of this solution is then checked by comparing the numerical strain rate at the vortex center with the theoretical prediction (Jiménez *et al.* 1996; Eloy & Le Dizès 1999). This 2D solution slightly evolves owing to viscous diffusion. This effect is known to influence the development of the elliptic instability (Eloy & Le Dizès 1999). For case (1), we have chosen to freeze artificially the base flow in order to identify more clearly the nonlinear effects on the instability. This choice is also motivated by applications of the results to larger Reynolds number flows for which viscous diffusion is negligible. Nevertheless, this assumption will be relaxed for the 2 counter-rotating vortex case. It will permit to check that it does not significantly influence the nonlinear dynamics of the instability.

For case (1), two sets of parameter are considered : $\varepsilon = 0.005$, $Re = \Gamma/\nu = 6300$ and $\varepsilon = 0.01$, $Re = 10000$. The nonlinear development of the elliptic instability is computed by simulating the Navier-Stokes equations for the perturbations using the 3D pseudo-spectral code. The size of the box along the vortex axis is such that it corresponds to a single wavelength of the most unstable linear mode. This mode is obtained from white noise by turning off the non-linear terms until the growth rate converges, and is then scaled to a small amplitude such that the linear growth of the instability is always observed before non-linear effects become significant.

For $\varepsilon = 0.005$, the onset of the elliptic instability is at $Re = 5416$. The first computation at $Re = 6300$ is performed close to the stability threshold in order to look at a weakly nonlinear regime. The linear growth rate at this Reynolds number is $\sigma = 1.9\,10^{-3}$. The evolution of the shape of the most unstable mode $k_z = 2.25$ is displayed in figure 13(a,b). While the linear eigenmode is perfectly aligned with the stretching axis (fig. 13(a)), the nonlinear effects cause a slight rotation of the structure, as predicted by the weakly nonlinear theory (Sipp 2000). The mode structure is almost not modified during this dynamics. The dynamics of the angle ϕ as defined in fig. 13(b) can be analyzed as the amplitude of the mode increases and is plotted in fig. 12. We observe a limit cycle with a small frequency approximatively equal to $8.6\,10^{-3}$. This behavior was predicted by Racz & Scott (2008) for the weakly nonlinear evolution of a similar instability in a cylin-

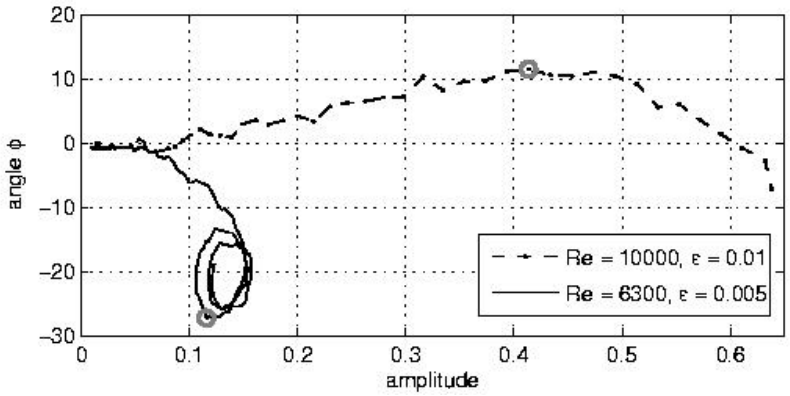

FIG. 12. Evolution of the angle (in degrees) and amplitude of the instability mode in the two cases. Solid line : $\varepsilon = 0.005$, $Re = 6300$. Dashed line : $\varepsilon = 0.01$, $Re = 10000$. The axial vorticity structure of the instability mode at the circles is shown in fig. 13.

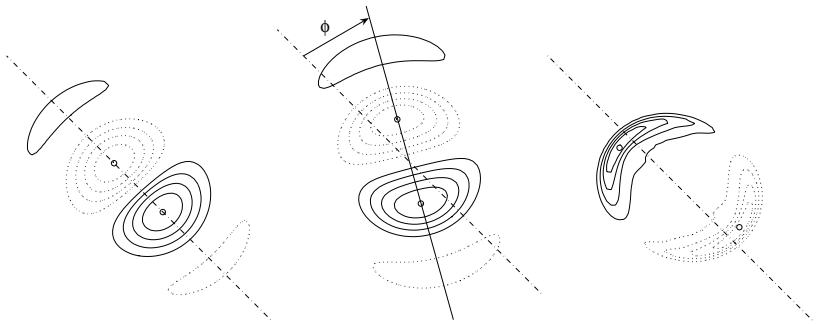

FIG. 13. Contour plot of the vorticity perturbation of the most unstable mode ($k_z = 2.25$) in the linear regime (a), $t = 960$ in case $\varepsilon = 0.005$, $Re = 6300$ (b), $t = 200$ in case $\varepsilon = 0.01$, $Re = 10000$ (c) corresponding to the angle and amplitude circled in fig. 12. Continuous line and dashed lines are positive and negative isovorticity contours respectively. The two circles indicate the maximum and minimum of each mode from which the angle ϕ is computed.

der, but it is observed for the first time in the case of the elliptic instability of a strained vortex. Note that in the inviscid framework, no limit cycle is expected in the weakly nonlinear regime : the angle should rotate toward the direction of compression of the strain field and the amplitude should return to zero (Sipp 2000). The time-evolution of the mean axial vorticity profile (z- and θ-averaged) is shown in fig. 14. The slow periodic oscillation associated with the limit cycle can be seen on this plot. Note also that the only effect of the perturbation is to flatten the mean profile near the vortex center. No effects are visible outside the vortex core contrarily to what we will now observe for the second set of parameters.

In the second simulation of case (1), we are much above threshold. The linear growth rate is now $\sigma = 1.08\,10^{-2}$, that is about 6 times higher than the previous case. The evolution of the energy of the different modes is plotted in figure 15. The unstable mode is growing as predicted by the linear theory (Le Dizès & Laporte 2002), and there is no visible departure from the linear growth until $t \simeq 120$, but the mode structure is not observed to rotate as in the previous case. The orientation angle slightly increases instead of decreasing as the amplitude grows (see fig. 12). This behavior was demonstrated as a possible weakly nonlinear regime(Racz & Scott 2008) but here it may also be due to the fact that we are far from threshold. Indeed, the mode structure is rapidly strongly modified (fig. 13(c)) such that the weakly nonlinear theory hypothesis is no longer

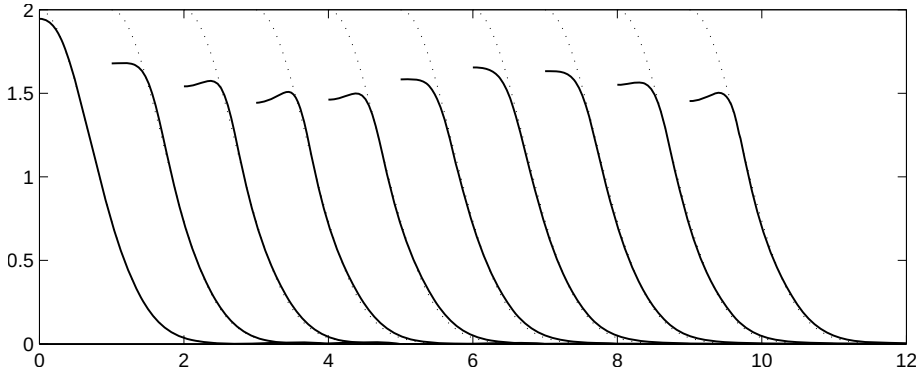

FIG. 14. Mean vorticity profiles (z and θ averaged) at different instants for the Lamb-Oseen vortex in a small strain field for $\varepsilon = 0.005$, $Re = 6300$. Profiles are separated by $\Delta t = 200$ (turnover time) and shifted by $\Delta r = 1$. (exception : between 4,5 and 6, $\Delta t = 100$). The first profile on the left is at $t = 0$ and the unperturbed profile is repeated in dotted style for reference.

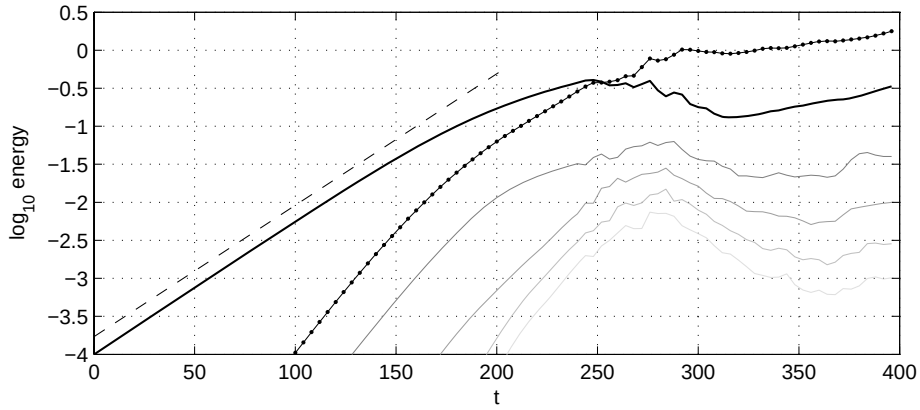

FIG. 15. Energy of the first seven modes as a function of time, showing the linear growth and saturation of the elliptic instability. The energy of the fundamental mode $k_z = 2.25$ and its successive harmonics are given by the plain black line and the gray-scale lines respectively ; the dotted line represents the energy of the $k_z = 0$ perturbation and the dashed line gives the slope of the linear growth. Case (1) for $\varepsilon = 0.01$, $Re = 10000$.

satisfied. The evolution becomes strongly nonlinear as illustrated in fig. 16 suggesting there is no saturation mechanism. In these snapshots, we clearly observe the formation of secondary vortex structures around the main vortex. These structures which resemble vortex loops move away from the vortex axis and become unstable. Small scales are then created but they are quickly damped by viscosity. After this disordered regime, the main vortex reforms, but because some vorticity has moved away from the initial vortex core, it is now much larger and has a weaker vorticity peak. This evolution can also be seen in fig. 17 where is displayed the mean vorticity profile as a function of time. Note that the formation of a thin layer on the mean vorticity profile is clearly visible on the fifth profile at $t = 240$. The trace of the expelled vortex structures observed in figs. 16(c,d) can also be associated with the secondary peak seen on the sixth profile.

The simulations of the two counter-rotating vortex system have been performed to check the robustness of the nonlinear scenario observed for case (1). In that case, the strain field responsible for the elliptic instability in each vortex is generated by the other vortex. Both the 2D simulations to obtain the basic flow and the 3D simulations of the perturbation equations have been performed with the 3D pseudo-spectral code. The 2D simulation was initialized by a field composed of

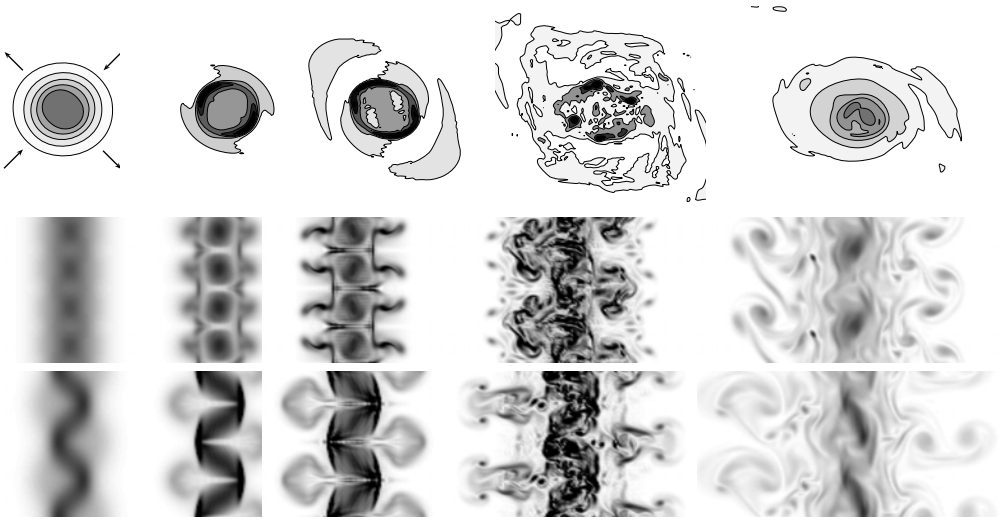

FIG. 16. Axially averaged vorticity contours in a plane perpendicular to the vortex axis (top) and total vorticity maps in longitudinal planes containing the vortex axis oriented along the direction of compression (middle) and of stretching (bottom) at different times (from left to right : $t = 120$, 200, 240, 280, 360). In the top snapshots, the spatial scale is the same for all snapshots, so is the color map which maps zero vorticity to white and $\omega = 2$ to black. The contours are equidistant vorticity levels ranging from minimum to maximum vorticity of each snapshot. For every longitudinal cuts, the color map (white for $\omega = 0$ to black for $\omega > 3$) and the spatial scale are the same.

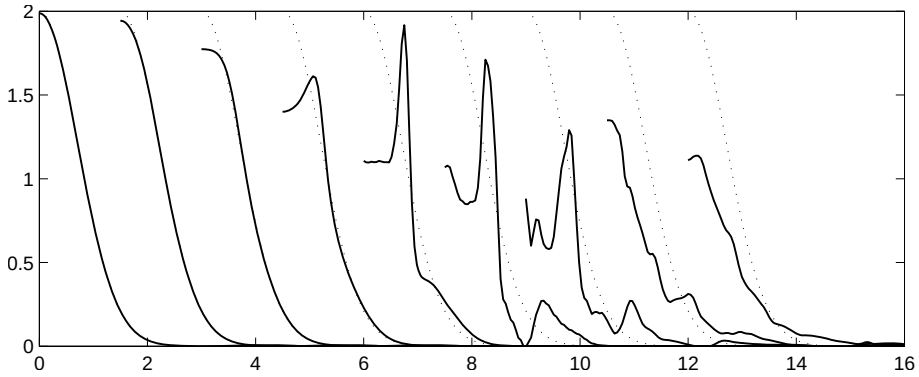

FIG. 17. Same as fig. 14 but for $\varepsilon = 0.01$ and $Re = 10000$. Profiles are here separated by $\Delta t = 40$ (turnover time) and shifted by $\Delta r = 1.5$. The first profile on the left is at $t = 80$.

two Lamb-Oseen vortices of opposite circulation $\pm\Gamma$, same radius a and separated by a distance b such that $Re = 6300$ and $b/a = 5$ at the end of the computation. For these parameters, the equivalent external strain rate is $\varepsilon = (a/b)^2 = 0.04$ and the linear growth rate is $\sigma = 4.2\,10^{-2}$, so that we are far from the instability threshold and strongly nonlinear evolution as in case (1) is expected. Counter-rotating vortex pairs are known to be also unstable to a long-wavelength instability (Crow instability). This instability is responsible for the formation of vortex rings (Leweke & Williamson 1998) and is expected to grow simultaneously with the short-wavelength elliptic instability we are interested in. Here Crow instability is filtered out by considering periodic boxes of small axial length. No interactions between both instabilities are therefore taken into account.

Contrarily to case (1), the base flow is now allowed to diffuse by viscosity during the nonlinear evolution of the perturbations. The 3D simulations are however initialized by the most unstable linear eigenmode of the base flow obtained at the end of the 2D simulation with a small amplitude

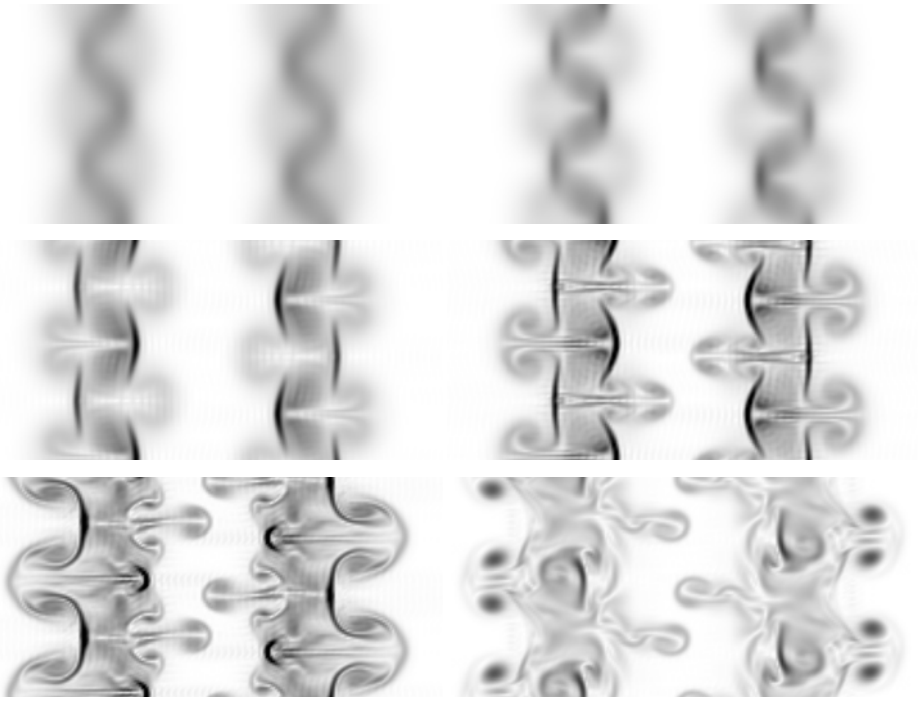

FIG. 18. Elliptic instability in vortex pairs. Total vorticity maps in the plane containing both vortex axes at different times (from left to right, top to bottom : $t = 22$, $t = 42$, $t = 62$, $t = 78$, $t = 88$, $t = 100$). The color scale goes from white ($\omega = 0$) to black ($\omega > 5$) and is the same in each snapshot.

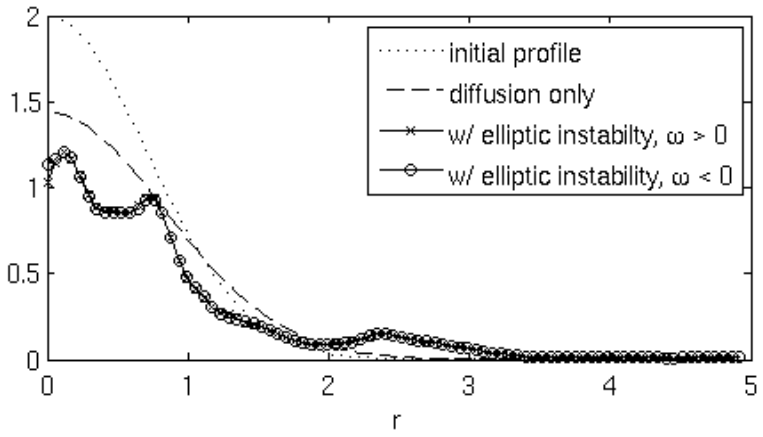

FIG. 19. Mean vorticity profiles (z and θ averaged) after 100 turnover times, obtained by diffusion only or with the action of elliptic instability, in the case of counter-rotating vortices. The profiles of the two vortices are almost the same.

(1%). The time-evolution of the total vorticity in the plane containing the vortex axes is shown in fig. 18. We can see that the nonlinear dynamics is qualitatively similar to what has been plotted in fig. 16. Thin layers of vorticity are formed at the periphery of the vortex and vortex loops are ejected from the vortex core (compare for example fig. 16(c) with figs. 18(c,d)). These secondary vorticity structures are then destabilized and dissipated by viscosity. The new vortices which form after this nonlinear evolution are, as for the single vortex case, larger and weaker (fig. 19).

The average profiles of the last snapshot ($t = 100$) are shown in figure 19 for each vortex. The vortex circulation is conserved but the radius computed from the second order moment of the distribution, gives $a = 1.68$ while a purely diffusive evolution would give $a_{diff} = 1.18$ at this Reynolds number. Alternatively, it would require 460 turnover times instead of 100 in order to obtain the same radius by diffusion only.

Other sets of parameters far above threshold have been considered for both the strained vortex and the two vortex configurations. They have all provided similar evolutions demonstrating the universality of the nonlinear dynamics of the elliptic instability without axial flow. Experiments for the two vortex system have been performed by Leweke & Williamson (1998) (see also Laporte & Leweke 2002). Unfortunately, they have not performed vorticity measurement in the late nonlinear regime. But their die visualizations (see fig. 19 of Leweke & Williamson (1998)) exhibit mushroom-like structures which resemble the expelled vorticity structure observed in fig. 18(d,e).

3.2. *Co-rotating vortices and merging*

In this section, we study the influence of the elliptic instability on the merging of two identical co-rotating vortices.

To quantify the influence of the instability, we have compared the merging of a purely 2D flow with that of a 3D flow with elliptic instability with and without axial jet. Values of the axial jet parameter corresponding to highly unstable modes have been chosen. The same numerical tools as before are used for the simulations and for each case, we use the following protocol :

(a) The two dimensional base flow is computed starting with two Gaussian vortices, separated by a large distance and we let the system evolve until the desired $(b/a)_0$ is obtained. The length scale is set to the new core size, so that we now have $a = 1$.

(b) From random noise, we let the most unstable mode evolve for 100 turnover times.

(c) The energy of the most unstable mode obtained by the previous step is set to $A^2 = 4.10^{-4}$ times the energy of the base flow.

(d) The full non-linear evolution of the flow is computed.

Although several values of W_0, Re and $(b/a)_0$ have been simulated, we document here only a few typical cases for $Re = 12500$. Two values of $(b/a)_0$, $(b/a)_0 = 5$ and $(b/a)_0 = 7$, corresponding to close vortices and distant vortices respectively, have been analyzed. And for each value of $(b/a)_0$, two or three values of W_0 have been computed and compared to the 3D simulation without axial flow and to the 2D simulation. For each 3D simulation, a particular axial wavelength close to the most unstable wavelength has been chosen. For example, for the simulations with $(b/a)_0 = 5$, we have taken $k_z a = 1.8, 3.0, 1.6$ for $W_0 = 0, 0.3, 0.6$ respectively. Typically, we have used the following spatial resolution for the 3D simulations. In the (x, y) plane, the grid spacing has been fixed to $\Delta = 0.07$ with 256×256 points, and on the z-axis we have used 5 harmonics of the most unstable mode (with a 2/3 rule anti-aliasing). We have checked on a few typical cases by using a much higher resolution along the z-axis, that the simulations performed with one mode with 5 harmonics were enough to capture correctly the main features of the nonlinear dynamics. Finally, note that we have also used a domain twice as large for the $k_z = 0$ flow (512×512 points) to avoid virtual images problems.

Let us first consider the configuration of close vortices ($(b/a)_0 = 5$). For this value of $(b/a)_0$, the temporal evolutions of the z-averaged vorticity profiles are displayed in the appendix A for the 2D case (left row), the 3D case with $W_0 = 0$ (middle row) and the 3D case with $W_0 = 0.6$ (right row). It is clearly seen in these snapshots that the dynamics of merging is different for each case. In the presence of the instability, merging occurs earlier than in the 2D case. This is also seen in figure 20 which shows the evolution of the separation distance b as a function of time. In

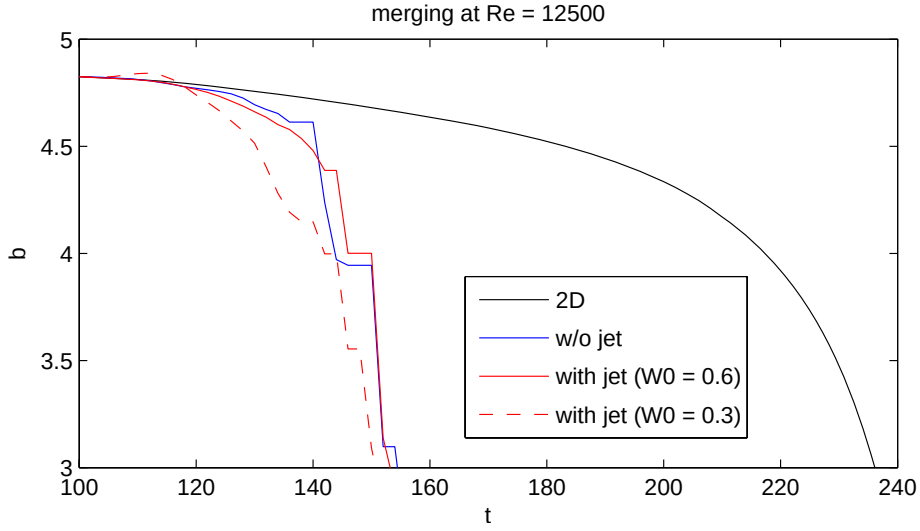

FIG. 20. Separation distance b between the two co-rotating vortices as a function of time, for $Re = 12500$, $(b/a)_0 = 5$.

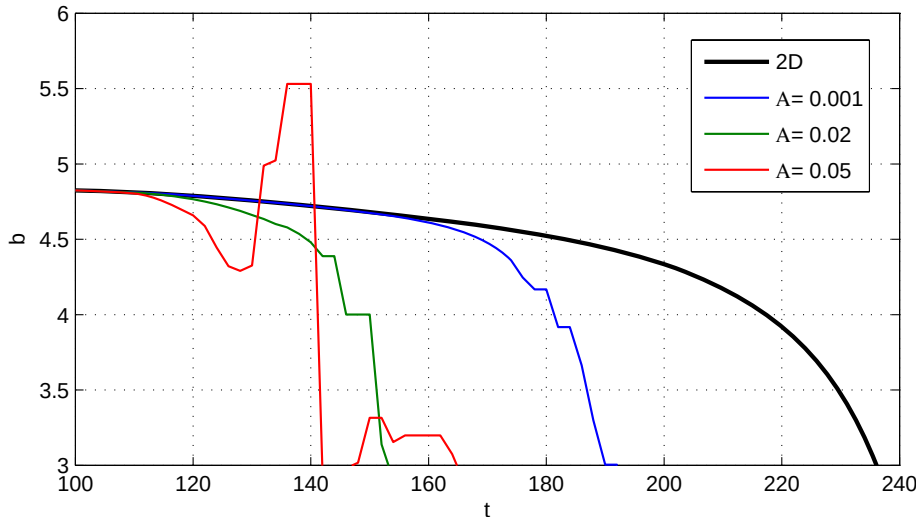

FIG. 21. Separation distance b between the two co-rotating vortices as a function of time, for $Re = 12500$, $W_0 = 0.6$ and different initial amplitudes A of the perturbation. Here $b_0 = 5$ and $a_0 = 1$.

this figure, we observe that the 3D merging with or without axial flow stars approximatively at the same time. We shall see below that this is related to the short initial separation distance of the vortices which is close to the 2D merging threshold. For short separation distances, we suspect that the linear growth of the instability which is comparable for both cases $W_0 = 0$ and $W_0 = 0.6$ is sufficient to initiate the merging process. However, if the amplitude of the perturbations at $t = 0$ is varied, the time to merging also changes. And as expected, merging happens earlier when the perturbation amplitude is larger (see fig. 21).

In the dynamics of wake vortices, it is also useful to analyze the shape of the vortex obtained after merging. Figure 22 shows that the merging with elliptic instability leads to weaker and wider vortices than the purely 2D merging. However, the variation of the final vortex profile does not vary monotonically with respect to the axial parameter. This is not surprising as the

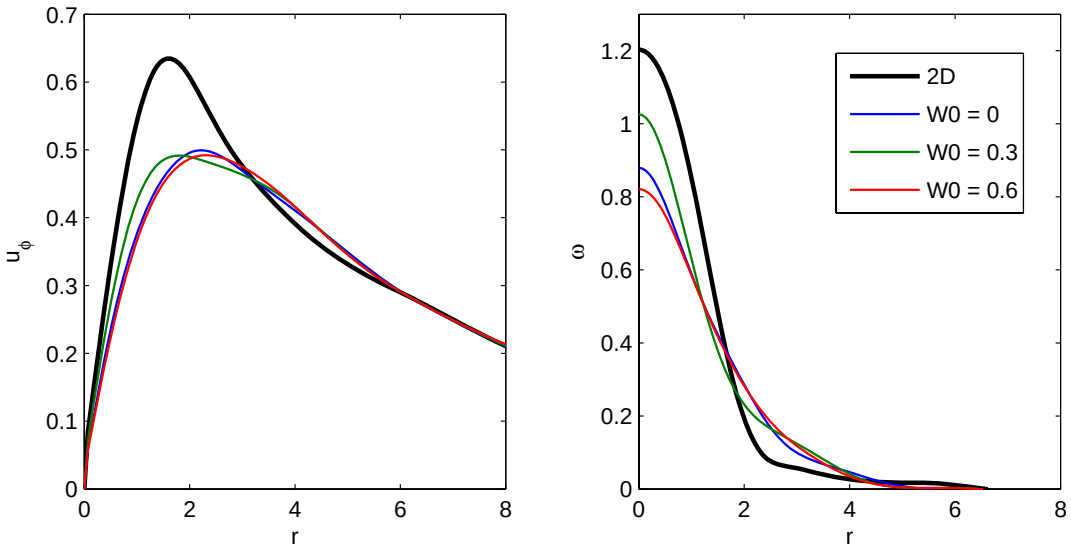

FIG. 22. Azimuthal velocity u_ϕ and axial vorticity ω profiles obtained after merging at $t = 500$, for $Re = 12500$, $(b/a)_0 = 5$.

instability characteristic does not vary that way either. The cases $W_0 = 0$ and $W_0 = 0.6$ are more unstable than the case $W_0 = 0.3$ (see fig. 2 for instance) which could explain the weaker effect of the instability for $W_0 = 0.3$.

W_0	b/a	a/b	Re	$k_z a$	$\sigma 2\pi a^2/\Gamma$	$t_m\Gamma/(2\pi a^2)$	$t_m\sigma$
0	7	0.143	10000	2.0	$5.0\,10^{-2}$	260	13
	8	0.125	12500	2.1	$3.3\,10^{-2}$	460	15
	9	0.111	12500	2.1	$2.5\,10^{-2}$	850	21
0.55	7	0.143	12500	1.75	$5.6\,10^{-2}$	520	29
0.53	8	0.125	12500	1.75	$4.0\,10^{-2}$	> 850	> 34
0.28	7	0.143	12500	2.96	$3.6\,10^{-2}$	> 850	> 30

TAB. 2. Frozen base flow simulations for different unstable modes and different separation distances. W_0 is the axial flow parameter, $k_z a$ is the axial wavelength of the computed main mode (computation also includes its harmonics), σ is the energy growth rate in the linear regime. t_m is the time at which merging starts.

Viscous diffusion, for the Reynolds numbers we are able to simulate, is important. It makes the vortex cores grow and therefore it always leads to merging, even when the elliptic instability is not present. In order to characterize more precisely the sole effect of the elliptic instability on merging, we have chosen to perform a few simulations in which the viscous diffusion of the base flow is turned off by freezing the base flow. By doing so, we also think that we are closer to the situations of aeronautical interest for which viscous diffusion is indeed negligible.

In the "frozen base flow" simulations, the merging when it occurs can only be due to the elliptic instability. In particular, when no instability develops, the flow remains unchanged and no merging can ever occur. However, when the instability is present, it may or may not lead to merging according to the nonlinear evolution of the instability. The simulations which are shown in the appendix B correspond to simulations with a frozen base flow. The initial separation distance is $(b/a)_0 = 7$. We are therefore far from the 2D merging threshold $a/b \approx 0.23$, that is $b/a \approx 4.35$. As no base flow diffusion is considered, the 2D case never merges. We can see in the snapshots shown in the appendix B that in the presence of the instability merging does occur. However, by contrast with the previous case, merging is clearly different for the three cases $W_0 = 0$, $W_0 = 0.3$ and $W_0 = 0.6$. In particular, merging is faster without axial flow. This has been observed for all the cases with $(b/a)_0 \geq 7$ we have simulated (see table 2). This can be linked to the fact that the growth of the core radius by the elliptic instability without axial flow is much more efficient than with axial flow.

This particular property has been analyzed by considering the development of the instability in a single frozen strained vortex. Typical results are displayed in figure 23 which shows the time evolution of the vortex radius for a few cases. We can note that the core radius of the case without jet can increase by more than 20% by the instability before saturating, whereas the radius increases by less than 10% for the case with jet, even for a strain field 3 times larger. After the relaminarization of the vortex, the instability can grow again, leading to a further increase of the vortex radius. This is what we observe for the case without jet in figure 23. It would have been also observed for the other cases if the simulations could have been performed up to longer times. In the snapshots shown in the appendix B, we can see that a single instability growth is enough to start an early vortex merging for the case without axial flow. However, this is not the same for the case with axial jet. Note for instance that for the case $W_0 = 0.5$, the instability grows up to $t \approx 150$, then the vortices relaminarize near $t \approx 250$, and the instability starts again at $t \approx 450$ and modifies sufficiently the vortices to initiate the merging.

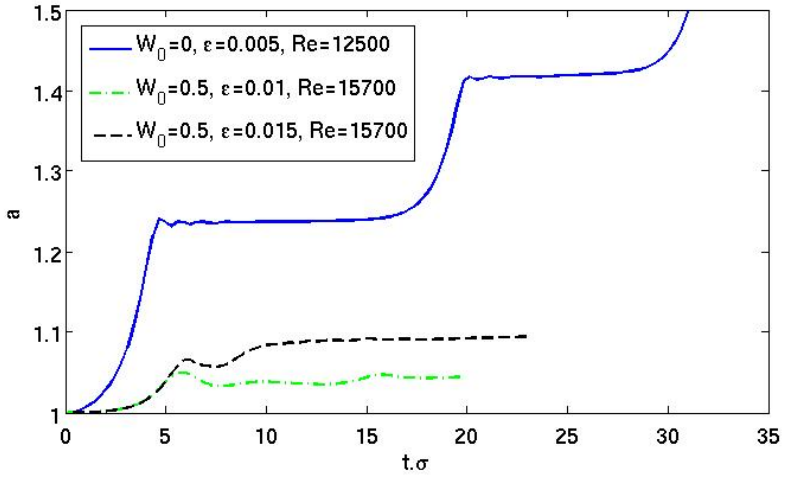

FIG. 23. Evolution of the vortex radius of a single vortex in a strain field due to the elliptic instability. Frozen base flow simulations.

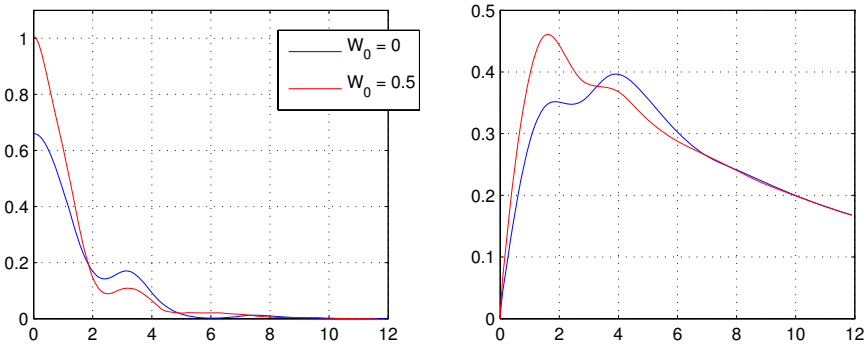

FIG. 24. Azimuthal velocity (left) and axial vorticity (right) profiles of the vortex obtained after merging for $Re = 12500$ and $(b/a)_0 = 7$, at $t = 700$. Frozen base flow simulations.

The final vortex profiles obtained after merging for the cases $W_0 = 0$ and $W_0 = 0.5$ are shown in figure 24. We can also see in this figure that the effect of the elliptic instability without jet is stronger. This has also been observed when viscous diffusion of the base flow was included as soon as the initial separation distance was sufficiently large. (Recall that no such difference was visible for $(b/a)_0 = 5$.) We have attributed this difference to the weaker growth of each vortex core by the elliptic instability in the presence of the axial flow.

Note finally that there is a second effect that could decrease the impact of the elliptic instability with axial jet : the axial flow parameter varies during the dynamics. For this reason, we may move from a value of W_0 for which the instability is favored to another for which the instability disappears or is weaker. This is never the case without axial flow, as W_0 remains null and thus always corresponds to a local peak of instability.

4. Conclusions

In the first part of this work, we have analyzed the linear stability of a co-rotating vortex pair with axial flow. We have demonstrated that new elliptic instability modes are destabilized

by axial flow. For small Reynolds numbers and small a/b, we have shown that the instability diagram resembles the theoretical prediction for counter-rotating vortices (Lacaze *et al.* 2007), although there are some explicit differences between these cases. When axial flow is progressively increased, the principal modes (combination of Kelvin modes of same radial branch label) of azimuthal wavenumbers $(-1,1)$ are stabilized and replace by other principal modes $(-2,0)$, $(-3,-1)$ and $(-4,-2)$. For large Reynolds numbers or large a/b, other instability modes have been observed and associated with a combination of Kelvin modes with different labels. These other modes are less unstable than the principal modes, whose characteristics are almost invariant. But they make the vortex pair unstable in a large wavenumber band whatever the axial flow.

In the second part of this work, we have demonstrated that without axial flow both weakly nonlinear and strongly nonlinear evolution of the elliptic instability were possible. The weakly nonlinear dynamics which has been observed very close to threshold is characterized by a limit cycle behavior. The strongly nonlinear dynamics, which has been obtained in most simulations, is much more violent but possesses some universal characteristic features. We have shown that it always follows the following steps : (1) concentration of the vorticity in thin layers at the periphery of the vortex, (2) expulsion of vortex loops, (3) breakdown of the whole structure, (4) relaminarisation process leading to the reformation of a weaker and larger vortex. We claim that this evolution is universal in high Reynolds number flows.

Naturally we have seen that this catastrophic evolution of the elliptic instability has a strong influence on merging for the case of co-rotating vortices. We have shown that vortex merging can be obtained thanks to the elliptic instability for a/b as small as 0.12. With axial flow, we have observed that the nonlinear dynamics of the elliptic instability is less violent. The growth of the vortex core size by the instability is also less important. As a consequence, co-rotating vortices with axial flow will merge sooner than 2D vortices but later than vortices without axial flow, especially if the initial separation distance is large. Moreover, the vortex obtained after merging is wider and weaker than the one obtained in 2D but thiner and stronger than in 3D without axial flow.

REFERENCES

BILLANT, P., BRANCHER, P. & CHOMAZ, J.-M. 1999 Three-dimensional stability of a vortex pair. *Phys. Fluids* **11**, 2069–2077.

ELOY, C. & LE DIZÈS, S. 1999 Three-dimensional instability of Burgers and Lamb-Oseen vortices in a strain field. *J. Fluid Mech.* **378**, 145–166.

ELOY, C., LE GAL, P. & LE DIZÈS, S. 2003 Elliptic and triangular instabilities in rotating cylinders. *J. Fluid Mech.* **476**, 357–388.

FABRE, D. & JACQUIN, L. 2004 Viscous instabilities in trailing vortices at large swirl numbers. *J. Fluid Mech.* **500**, 239–262.

FABRE, D., SIPP, D. & JACQUIN, L. 2006 The Kelvin waves and the singular modes of the Lamb-Oseen vortex. *J. Fluid Mech.* **551**, 235–274.

JIMÉNEZ, J., MOFFATT, H. K. & VASCO, C. 1996 The structure of the vortices in freely decaying two dimensional turbulence. *J. Fluid Mech.* **313**, 209–222.

KERSWELL, R. R. 2002 Elliptical instability. *Annu. Rev. Fluid Mech.* **34**, 83–113.

LACAZE, L., BIRBAUD, A.-L. & LE DIZÈS, S. 2005 Elliptic instability in a Rankine vortex with axial flow. *Phys. Fluids* **17** (017101).

LACAZE, L., RYAN, K. & LE DIZÈS, S. 2007 Elliptic instability in a strained Batchelor vortex. *J. Fluid Mech.* **577**, 341–361.

LAPORTE, F. & LEWEKE, T. 2002 Elliptic instability of trailing vortices : experiment and direct numerical simulation. *AIAA Journal* **40** (12), 2483–2494.

LE DIZÈS, S. 2004 Viscous critical-layer analysis of vortex normal modes. *Stud. Appl. Math.* **112** (4), 315–332.

LE DIZÈS, S. & LACAZE, L. 2005 An asymptotic description of vortex Kelvin modes. *J. Fluid Mech.* **542**, 69–96.

LE DIZÈS, S. & LAPORTE, F. 2002 Theoretical predictions for the elliptic instability in a two-vortex flow. *J. Fluid Mech.* **471**, 169–201.

LE DIZÈS, S. & VERGA, A. 2002 Viscous interaction of two co-rotating vortices before merging. *J. Fluid Mech.* **467**, 389–410.

LEWEKE, T. & WILLIAMSON, C. H. K. 1998 Cooperative elliptic instability of a vortex pair. *J. Fluid Mech.* **360**, 85–119.

MEUNIER, P., LE DIZÈS, S. & LEWEKE, T. 2005 Physics of vortex merging. *C. R. Physique* **6**, 431–450.

MEUNIER, P. & LEWEKE, T. 2005 Elliptic instability of a co-rotating vortex pair. *J. Fluid Mech.* **533**, 125–159.

OTHEGUY, P., CHOMAZ, J.-M. & BILLANT, P. 2006 Elliptic and zigzag instabilities on co-rotating vertical vortices in a stratified fluid. *J. Fluid Mech.* **553**, 253–272.

PRADEEP, D. S. & HUSSAIN, F. 2004 Effects of boundary condition in numerical simulations of vortex dynamics. *J. Fluid Mech.* **516**, 115–124.

RACZ, J.-P. & SCOTT, J. F. 2008 Parametric instability in a rotating cylinder of gas subject to sinusoidal axial compression. Part 2. Weakly nonlinear theory. *J. Fluid Mech.* **595**, 291–321.

ROY, C., SCHAEFFER, N., LE DIZÈS, S. & THOMPSON, M. 2008 Stability of a pair of co-rotating vortices with axial flow. *Phys. Fluids* (submitted).

RYAN, K., THOMPSON, M. C. & HOURIGAN, K. 2005 Three-dimensional transition in the wake of elongated bluff bodies. *J. Fluid Mech.* **538**, 1–29.

SAFFMAN, P. G. 1992 *Vortex dynamics*. Cambridge University Press.

SCHAEFFER, N. & LE DIZÈS, S. 2008 Nonlinear dynamics of the elliptic instability. *Submitted to Phys. Rev. Letters* .

SIPP, D. 2000 Weakly nonlinear saturation of short-wave instabilities in a strained Lamb-Oseen vortex. *Phys. Fluids* **12** (7), 1715–1729.

THOMPSON, M. C., HOURIGAN, K. & SHERIDAN, J. 1996 Three-dimensional instabilities in the wake of a circular cylinder. *Experimental Thermal and Fluid Science* **12**, 190–196.

THOMPSON, M. C., LEWEKE, T. & PROVANSAL, M. 2001 Kinematics and dynamics of sphere wake transition. *J. Fluids Struct.* **15**, 575–585.

VINCENT, A. & MENEGUZZI, M. 1991 The spatial structure and statistical properties of homogeneous turbulence. *J. Fluid Mech.* **225**, 1–20.

WALEFFE, F. 1989 The 3d instability of a strained vortex and its relation to turbulence. PhD thesis, Massachusetts Institute of Technology.

Annexe A. Temporal evolution of vortex merging for $(b/a)_0 = 5$ and $Re = 12500$.

In the following pages, the dynamics of merging of two identical vortices is represented as a series of pictures, for $Re = 12500$ and an initial separation distance $(b/a)_0 = 5$. Each line is a different time, and each row a different simulation. The 2D simulation shown on the left row, is compared to the 3D cases without axial flow (middle row) and with $W_0 = 0.6$ (right row). Time is normalized by the characteristic time scale of each vortex : $2\pi a_0^2/\Gamma$.

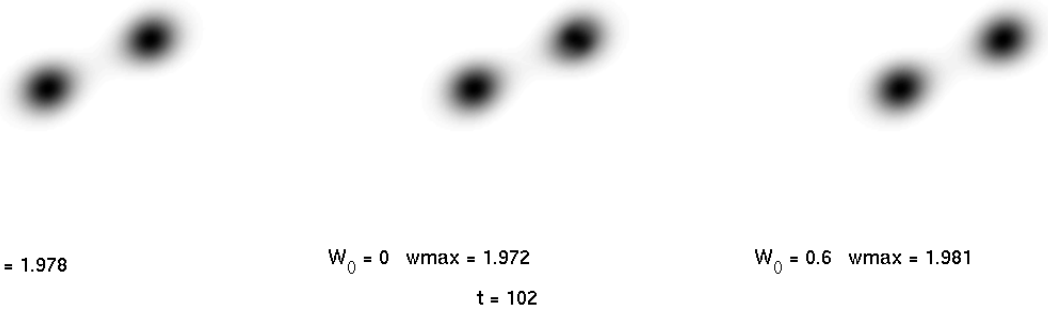

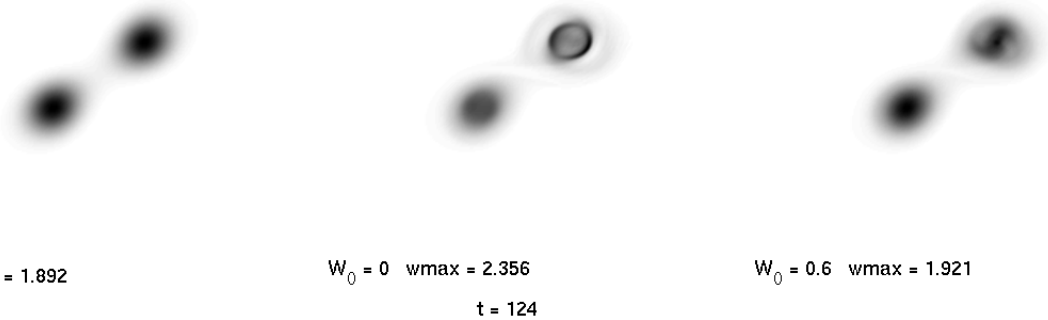

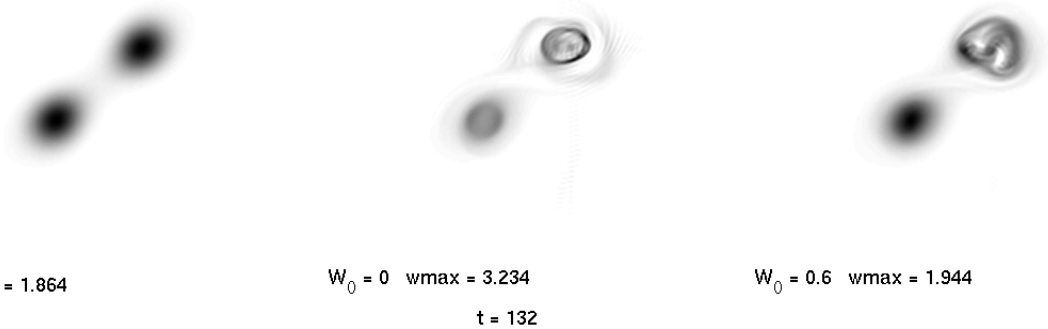

2D wmax = 1.85 | W_0 = 0 wmax = 3.606 t = 136 | W_0 = 0.6 wmax = 2.137

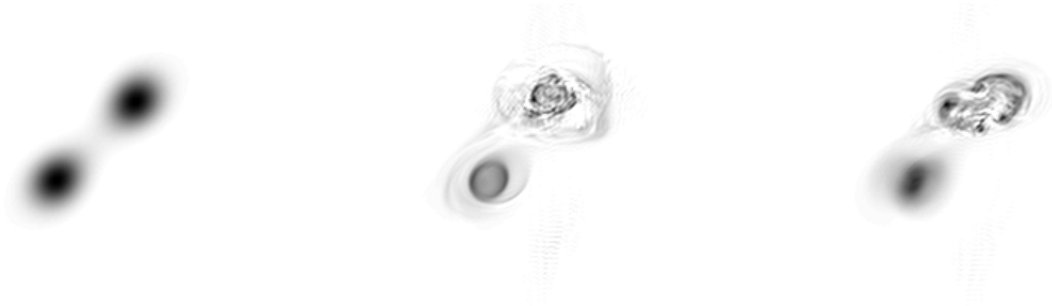

2D wmax = 1.835 | W_0 = 0 wmax = 3.027 t = 140 | W_0 = 0.6 wmax = 2.45

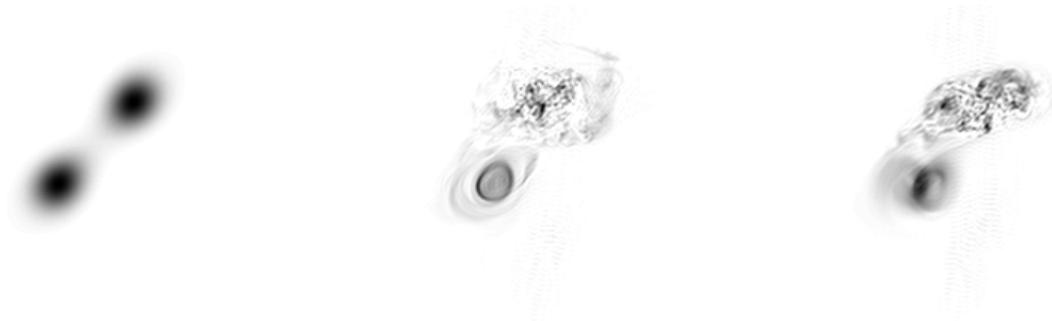

2D wmax = 1.821 | W_0 = 0 wmax = 3.258 t = 144 | W_0 = 0.6 wmax = 2.275

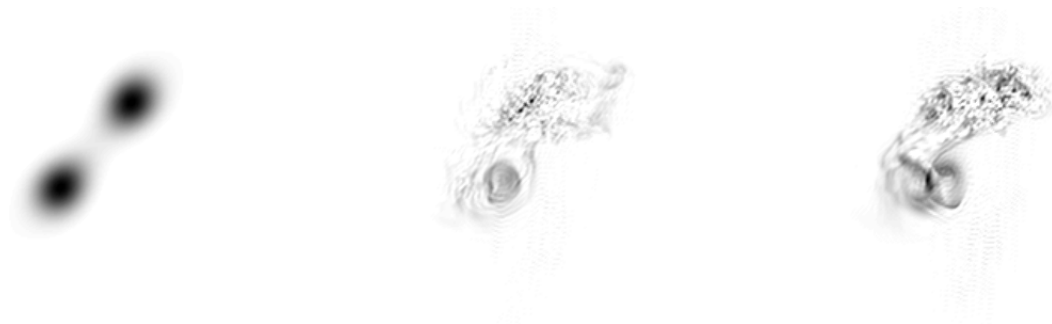

2D wmax = 1.805 | W_0 = 0 wmax = 4.554 t = 148 | W_0 = 0.6 wmax = 2.662

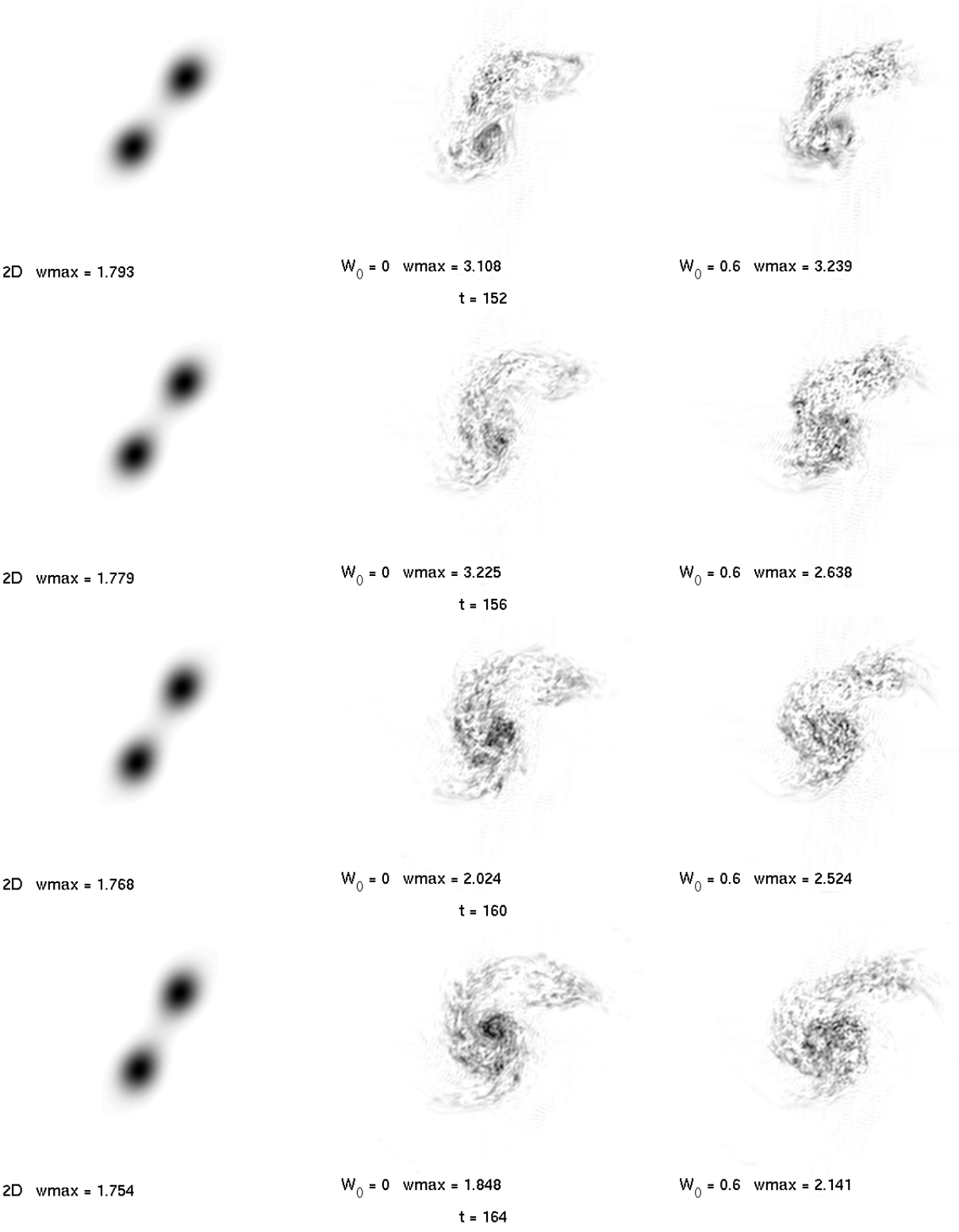
2D wmax = 1.793
W0 = 0 wmax = 3.108
t = 152
W0 = 0.6 wmax = 3.239
2D wmax = 1.779
W0 = 0 wmax = 3.225
t = 156
W0 = 0.6 wmax = 2.638
2D wmax = 1.768
W0 = 0 wmax = 2.024
t = 160
W0 = 0.6 wmax = 2.524
2D wmax = 1.754
W0 = 0 wmax = 1.848
t = 164
W0 = 0.6 wmax = 2.141

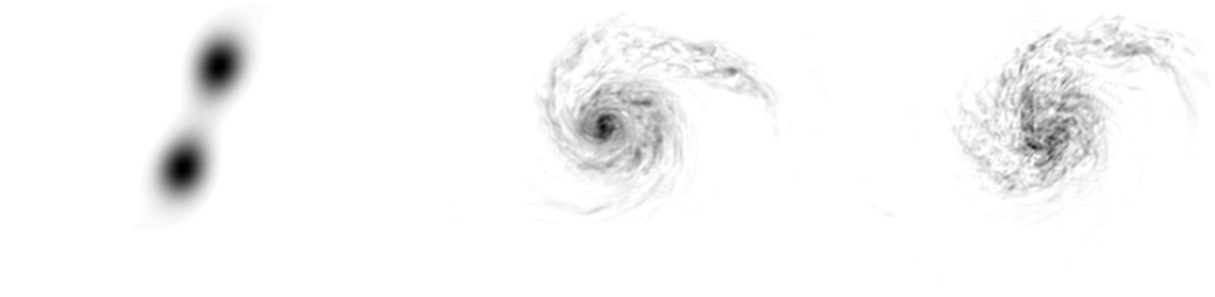

2D wmax = 1.723 | W_0 = 0 wmax = 1.985 | W_0 = 0.6 wmax = 2.017

t = 174

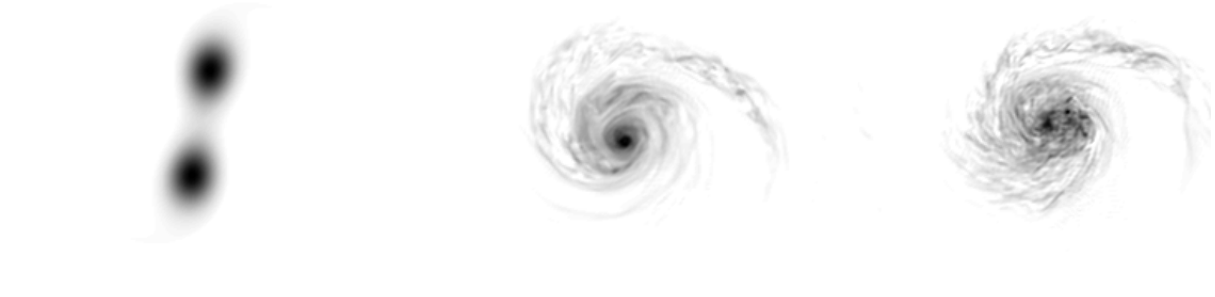

2D wmax = 1.691 | W_0 = 0 wmax = 1.745 | W_0 = 0.6 wmax = 1.524

t = 184

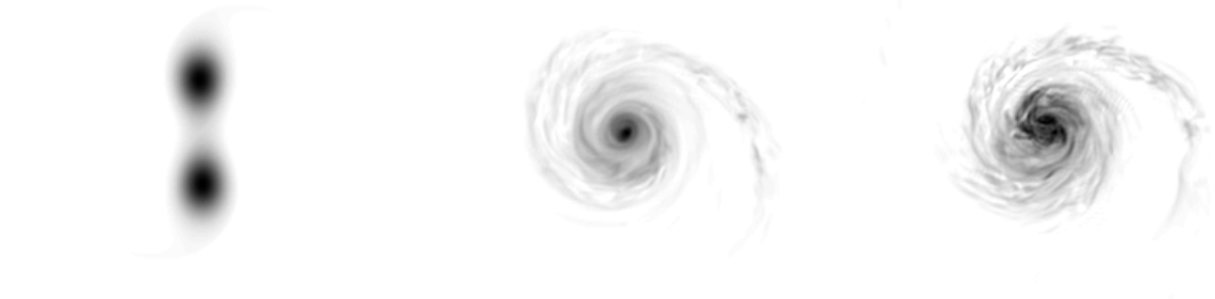

2D wmax = 1.662 | W_0 = 0 wmax = 1.75 | W_0 = 0.6 wmax = 1.193

t = 194

2D wmax = 1.545 | W_0 = 0 wmax = 1.396 | W_0 = 0.6 wmax = 1.22

t = 236

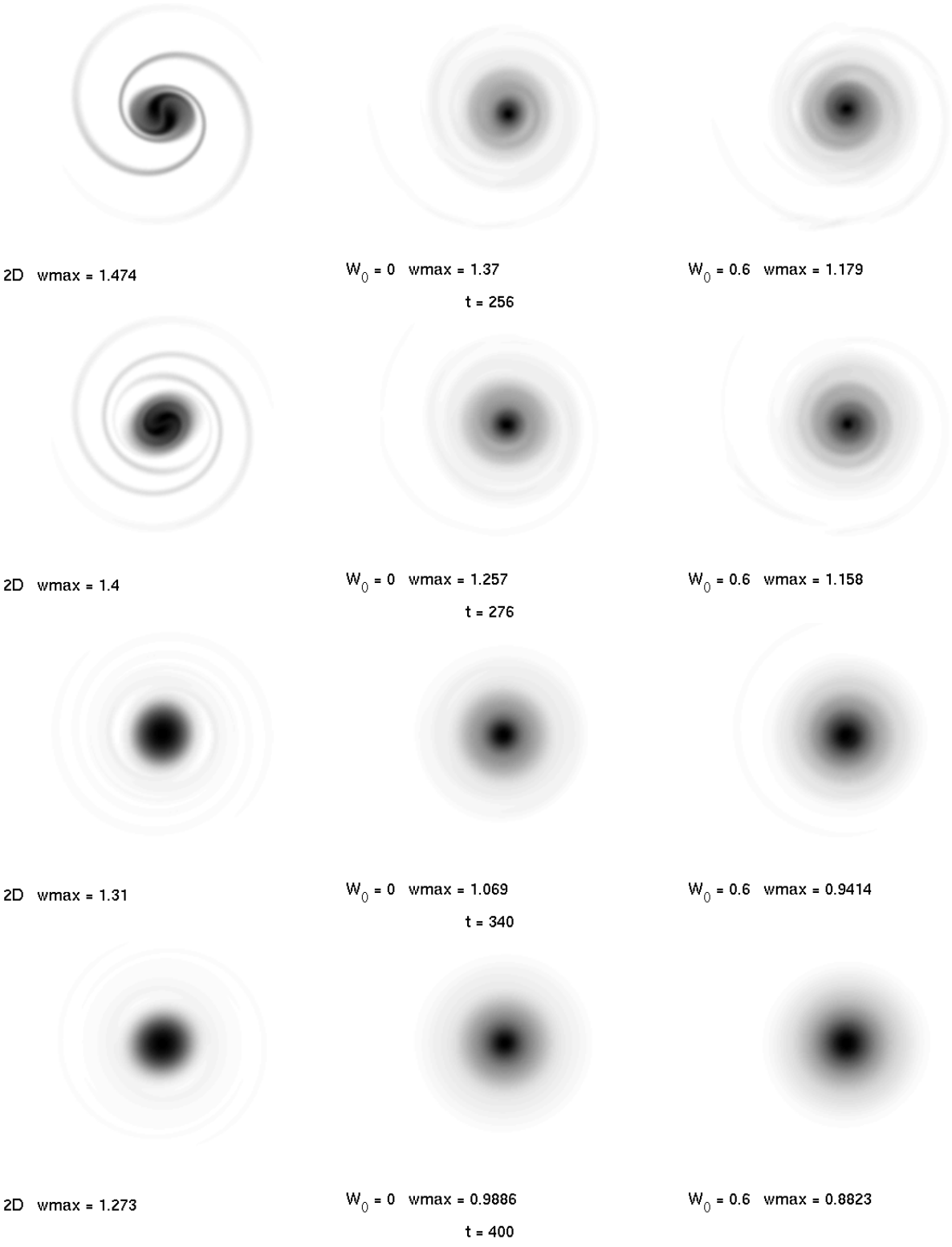
2D wmax = 1.474
W0 = 0 wmax = 1.37
t = 256
W0 = 0.6 wmax = 1.179
2D wmax = 1.4
W0 = 0 wmax = 1.257
t = 276
W0 = 0.6 wmax = 1.158
2D wmax = 1.31
W0 = 0 wmax = 1.069
t = 340
W0 = 0.6 wmax = 0.9414
2D wmax = 1.273
W0 = 0 wmax = 0.9886
t = 400
W0 = 0.6 wmax = 0.8823

Annexe B. Temporal evolution of vortex merging with a frozen base flow for $(b/a) = 7$ and $Re = 12500$.

In the following pages, the dynamics of merging of two identical vortices is displayed in a series of pictures for $Re = 12500$ and an initial separation distance $(b/a)_0 = 7$. The viscous diffusion of the base flow has been artificially suppressed. As above, each line is a different time, and each row a different simulation corresponding to a specific value of W_0.

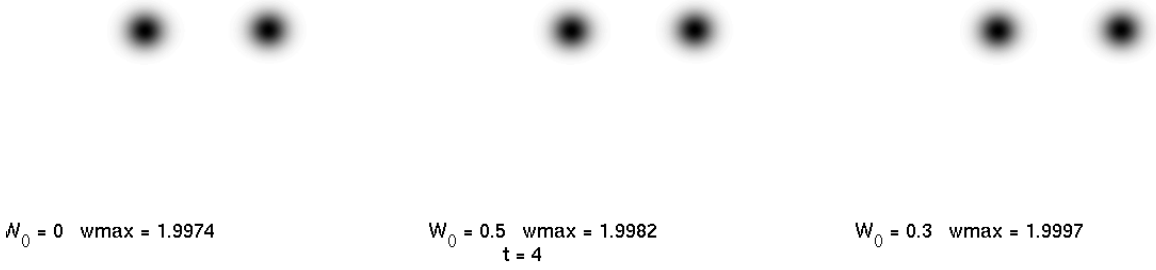

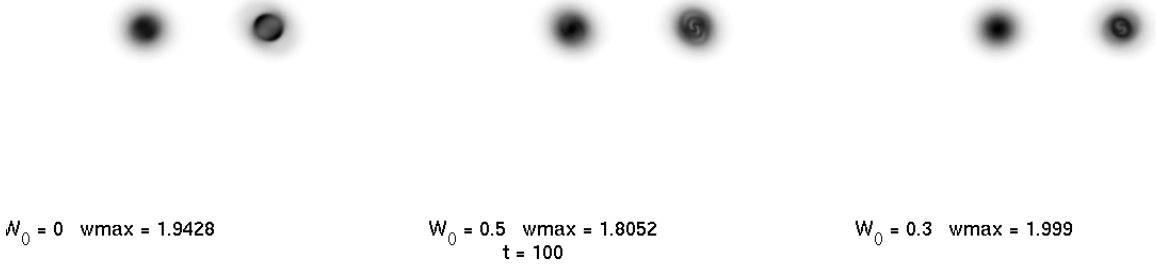

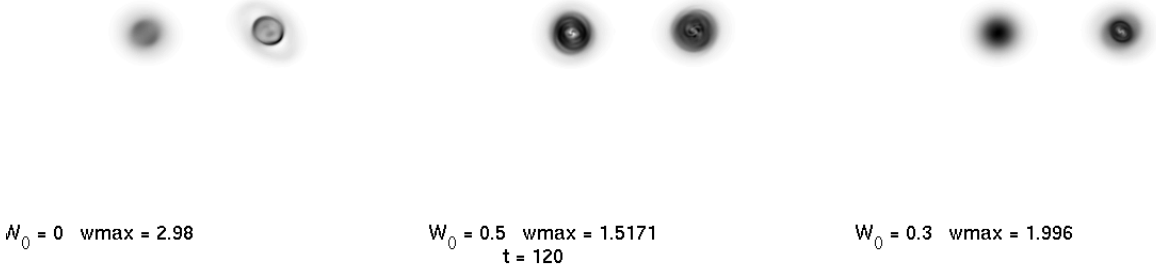

W_0 = 0 wmax = 4.884

W_0 = 0.5 wmax = 1.9064
t = 140

W_0 = 0.3 wmax = 1.9748

W_0 = 0 wmax = 2.956

W_0 = 0.5 wmax = 2.3297
t = 160

W_0 = 0.3 wmax = 2.0905

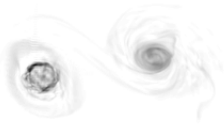

W_0 = 0 wmax = 3.906

W_0 = 0.5 wmax = 3.201
t = 180

W_0 = 0.3 wmax = 1.7888

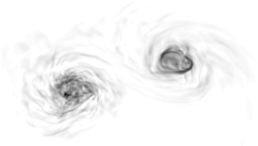

W_0 = 0 wmax = 2.6402

W_0 = 0.5 wmax = 2.5162
t = 200

W_0 = 0.3 wmax = 1.7897

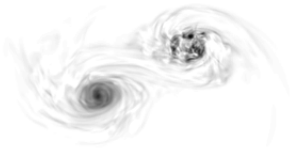

W_0 = 0 wmax = 2.0941

W_0 = 0.5 wmax = 3.022
t = 220

W_0 = 0.3 wmax = 1.8554

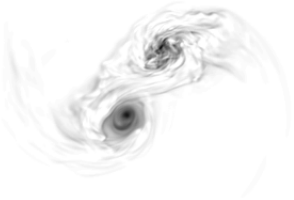

W_0 = 0 wmax = 1.846

W_0 = 0.5 wmax = 2.3649
t = 240

W_0 = 0.3 wmax = 1.9702

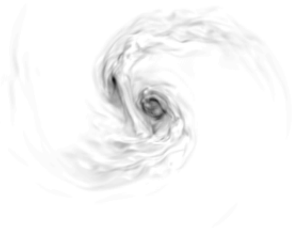

W_0 = 0 wmax = 1.9272

W_0 = 0.5 wmax = 2.53
t = 260

W_0 = 0.3 wmax = 1.7405

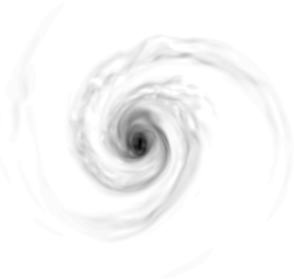

W_0 = 0 wmax = 1.3725

W_0 = 0.5 wmax = 2.0714
t = 280

W_0 = 0.3 wmax = 1.5304

W_0 = 0 wmax = 1.2935 | W_0 = 0.5 wmax = 2.1145 t = 300 | W_0 = 0.3 wmax = 1.4746

W_0 = 0 wmax = 1.04 | W_0 = 0.5 wmax = 1.7027 t = 360 | W_0 = 0.3 wmax = 1.4401

W_0 = 0 wmax = 0.96525 | W_0 = 0.5 wmax = 1.5013 t = 400 | W_0 = 0.3 wmax = 1.3573

W_0 = 0 wmax = 0.88801 | W_0 = 0.5 wmax = 1.2241 t = 440 | W_0 = 0.3 wmax = 1.2572

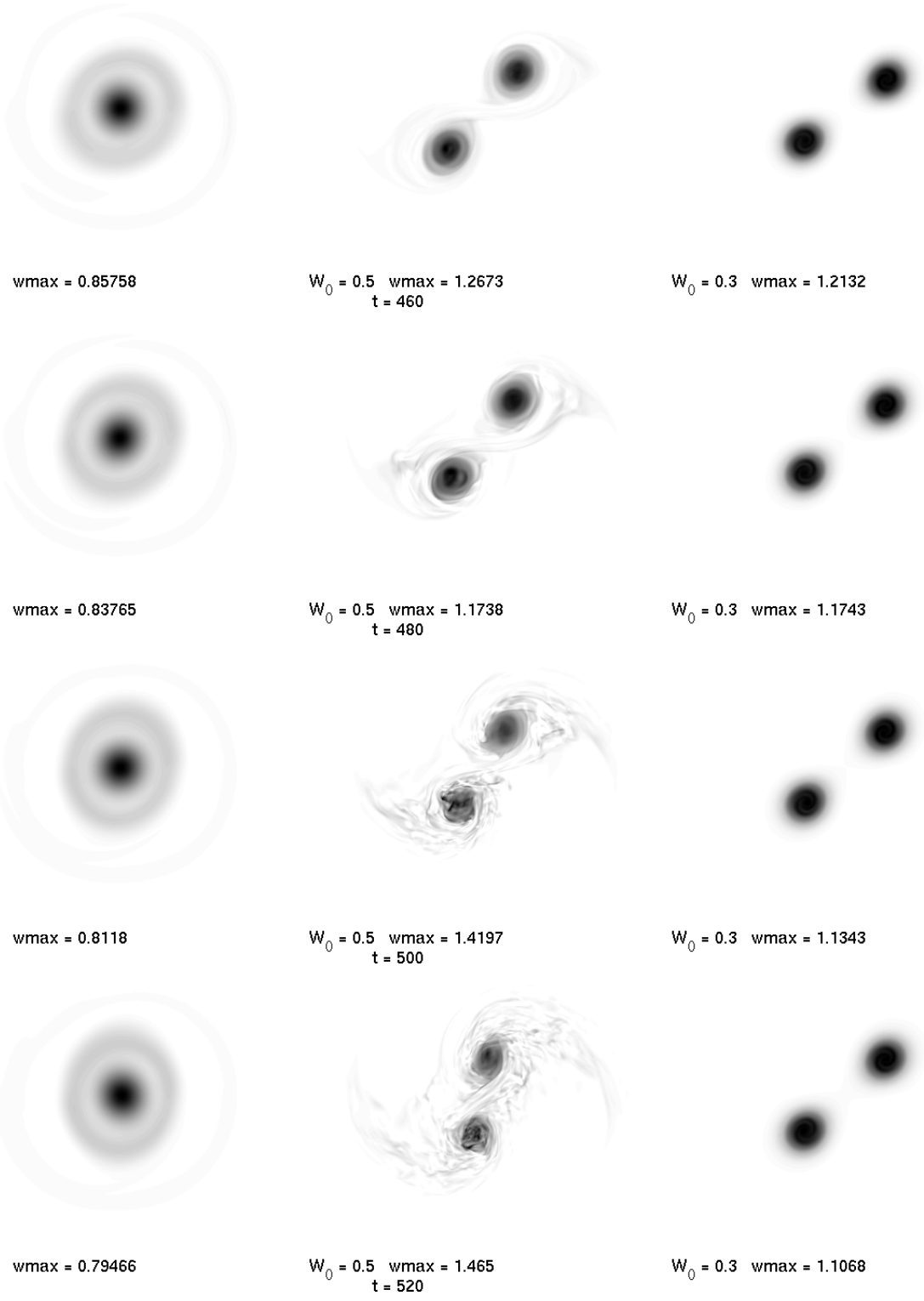
W0 = 0 wmax = 0.85758
W0 = 0.5 wmax = 1.2673
t = 460
W0 = 0.3 wmax = 1.2132
W0 = 0 wmax = 0.83765
W0 = 0.5 wmax = 1.1738
t = 480
W0 = 0.3 wmax = 1.1743
W0 = 0 wmax = 0.8118
W0 = 0.5 wmax = 1.4197
t = 500
W0 = 0.3 wmax = 1.1343
W0 = 0 wmax = 0.79466
W0 = 0.5 wmax = 1.465
t = 520
W0 = 0.3 wmax = 1.1068

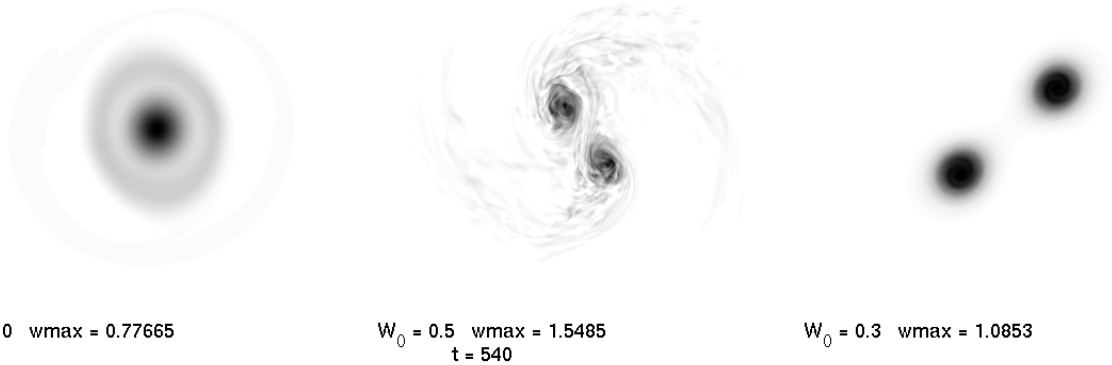

W_0 = 0 wmax = 0.77665 | W_0 = 0.5 wmax = 1.5485 t = 540 | W_0 = 0.3 wmax = 1.0853

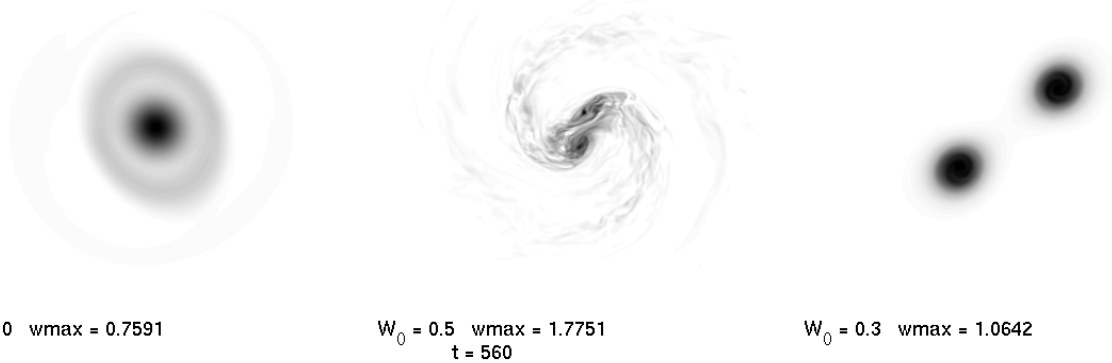

W_0 = 0 wmax = 0.7591 | W_0 = 0.5 wmax = 1.7751 t = 560 | W_0 = 0.3 wmax = 1.0642

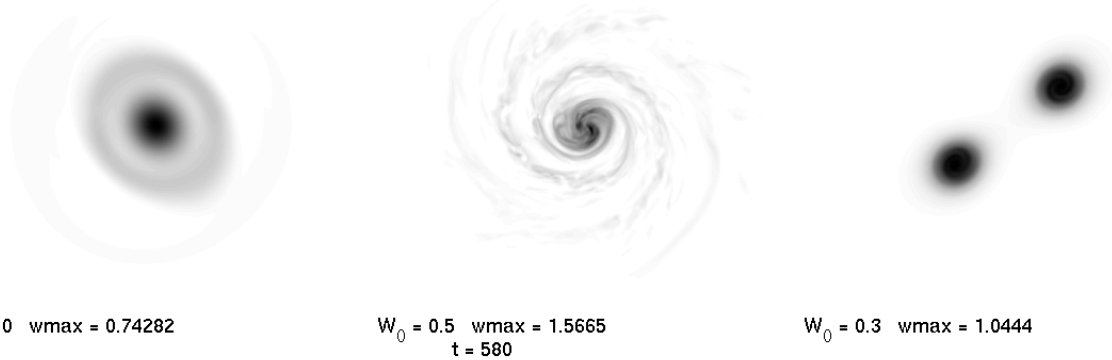

W_0 = 0 wmax = 0.74282 | W_0 = 0.5 wmax = 1.5665 t = 580 | W_0 = 0.3 wmax = 1.0444

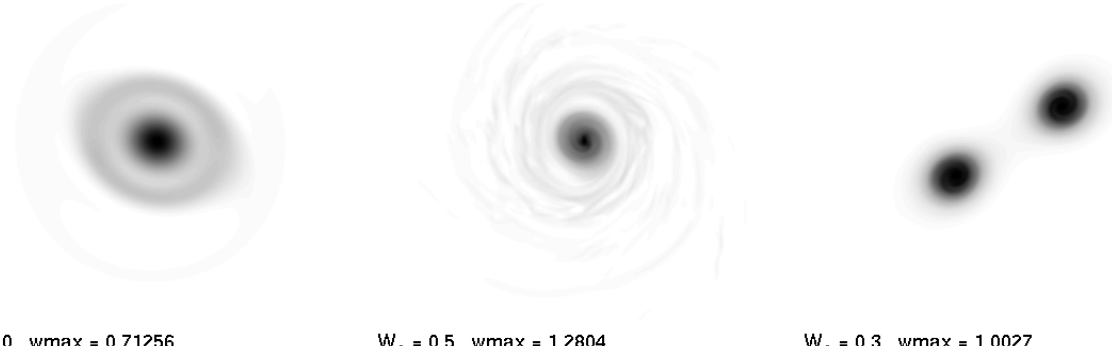

W_0 = 0 wmax = 0.71256 | W_0 = 0.5 wmax = 1.2804 t = 620 | W_0 = 0.3 wmax = 1.0027

W_0 = 0 wmax = 0.67425 | W_0 = 0.5 wmax = 1.0565 t = 680 | W_0 = 0.3 wmax = 0.93867

W_0 = 0 wmax = 0.66142 | W_0 = 0.5 wmax = 1.0263 t = 700 | W_0 = 0.3 wmax = 0.91197

W_0 = 0 wmax = 0.65071 | W_0 = 0.5 wmax = 0.99252 t = 720 | W_0 = 0.3 wmax = 0.907

W_0 = 0 wmax = 0.6395 | W_0 = 0.5 wmax = 0.95768 t = 740 | W_0 = 0.3 wmax = 2.2745

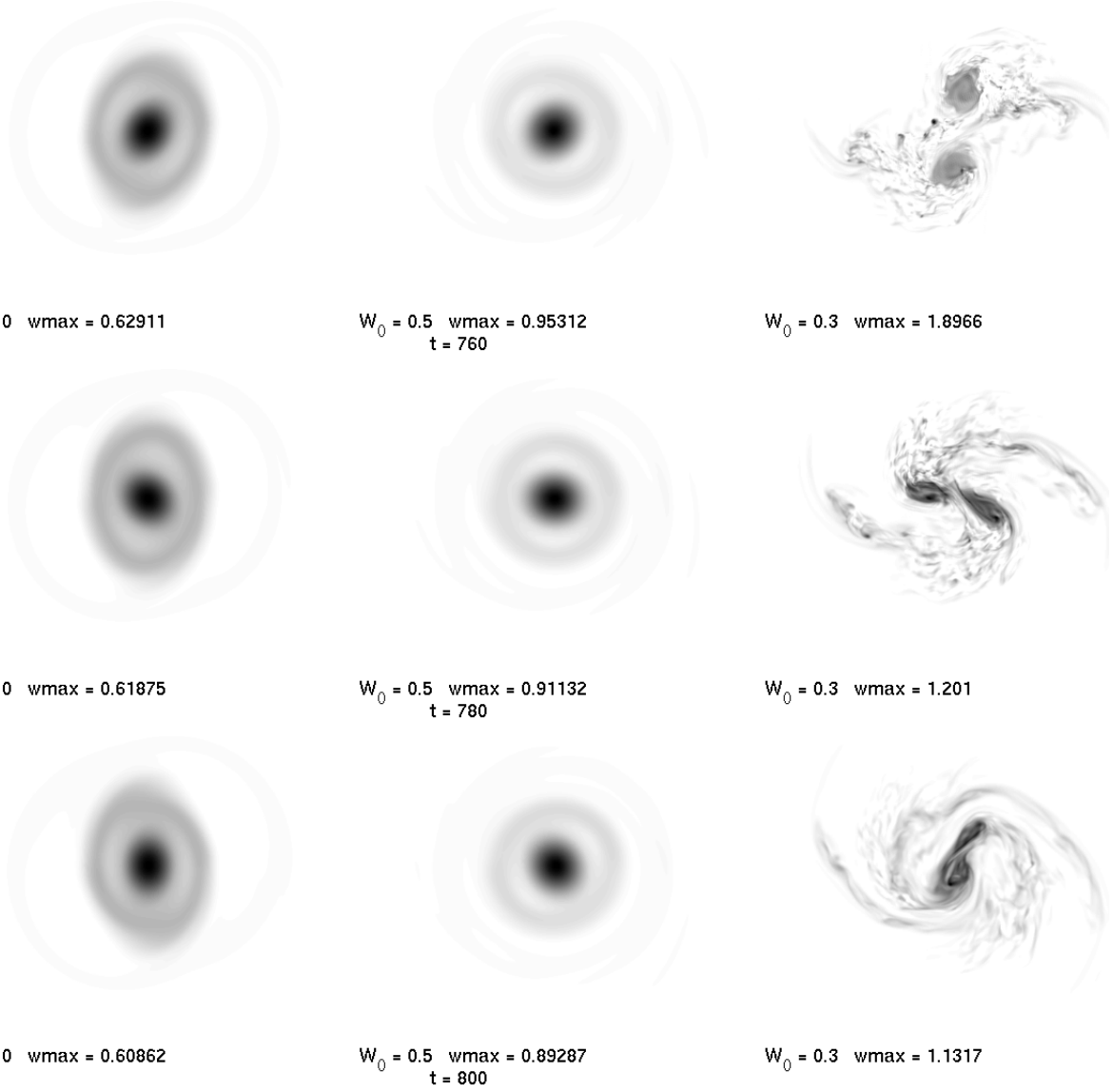
W0 = 0 wmax = 0.62911
W0 = 0.5 wmax = 0.95312
t = 760
W0 = 0.3 wmax = 1.8966
W0 = 0 wmax = 0.61875
W0 = 0.5 wmax = 0.91132
t = 780
W0 = 0.3 wmax = 1.201
W0 = 0 wmax = 0.60862
W0 = 0.5 wmax = 0.89287
t = 800
W0 = 0.3 wmax = 1.1317